Noninteger Lexicographic-Optimization-Based Sequential Model-Predictive Fault-Tolerant Control of T-Type Shunt Active Power Filter

Bo Long, *Senior Member, IEEE*, TianXu Cao, *Student Member, IEEE*, XinYue Qi, DaWei Shen, Josep M. Guerrero, *Fellow, IEEE*, José Rodríguez, *Life Fellow, IEEE*, and Kil To Chong, *Member, IEEE*

***Abstract*—Fault-tolerant control (FTC) strategies have been proposed to improve the reliability of power electronic systems. However, the FTC of the three-level T-type converter based shunt active power filter (SAPF) remains limited by redundant devices. To address this problem, an FTC strategy called sequential model predictive tolerant control (SMPTC) is combined with a nonintegral lexicographic optimization (LO) algorithm for solving multiobjective optimization problems. First, the power circuit, space voltage vector diagram, harmonic extraction, and prediction models of the SAPF system are introduced. Second, based on power-switch fault analysis, an adaptive dc bus voltage regulation method is proposed, which ensures that the candidate voltage vectors are fully utilized in the fault state. Third, an LO-SMPTC strategy is proposed by designing a sequential predictive controller that considers the neutral point (NP) voltage and the tracking of the SAPF output current. Compared with the traditional model predictive control, the proposed method not only achieves NP voltage balance and excellent harmonic compensation but also eliminates the selection of weighting factors, thereby improving the control flexibility and time efficiency. Finally, the effectiveness of the LO-SMPTC on the dc bus voltage, NP voltage oscillations, grid current power quality, and pole voltage under different scenarios is demonstrated through experiments.**

***Index Terms*—Lexicographic optimization (LO), neutral-point voltage balance, predictive tolerant control, shunt active power filter (SAPF).**

Manuscript received October 20, 2021; revised December 3, 2021; accepted December 8, 2021. Date of publication December 13, 2021; date of current version February 18, 2022. This work was supported in part by the Fundamental Research Funds for the Central Universities of China under Grant ZYGX2019J033, in part by the Key R&D Plan of Science and Technology Department of Sichuan Province under Grant 20ZDYF2816, in part by the State Key Laboratory of Control and Simulation of Power System Generation Equipment, China, under Grant SKLD20M11, in part by Tsinghua University, China, in part by the Guangdong Basic and Applied Basic Research Foundation under Grant 2021A1515010666, and in part by the Center for Research on Microgrids (CROM), Velux Foundations, through the VILLUM Investigator under Grant 25920. The work of J. Rodriguez was supported by ANID under Projects FB0008, ACT192013, and 1210208. Recommended for publication by Associate Editor A. Lindemann. *(Corresponding authors: Tianxu Cao; Kil To Chong.)*

Bo Long, TianXu Cao, and XinYue Qi are with the School of Mechanical and Electrical Engineering, Institute for Electric Vehicle Driving System and Safety Technology, University of Electronic Science and Technology of China, Chengdu 611731, China, with Yangtze Delta Region Institute, University of Electronic Science and Technology of China, Huzhou 313001, China, and also with the Institute of Electronic and Information Engineering, University of Electronic Science and Technology of China, Guangdong 523808, China (e-mail: longbouestc1980@126.com; caotxuestc@163.com; dbl1099246745@mail.nwpu.edu.cn).

DaWei Shen is with the School of Mechatronics and Electrical Engineering, University of Electronic Science and Technology of China, Chengdu 710049, China (e-mail: shendaweii@163.com).

Josep M. Guerrero is with the Department of Energy Technology, Aalborg University, 9220 Aalborg, Denmark (e-mail: joz@et.aau.dk).

José Rodríguez is with the Faculty of Engineering, Universidad Andres Bello, Santiago 8370146, Chile (e-mail: jose.rodriguez@unab.cl).

Kil To Chong is with the Department of Electronics and Information Engineering, Jeonbuk National University, Jeonju 54896, South Korea (e-mail: kitchong@jbnu.ac.kr).

Color versions of one or more figures in this article are available at https://doi.org/10.1109/TPEL.2021.3134712.

Digital Object Identifier 10.1109/TPEL.2021.3134712

I. Introduction

With the development of power-electronic-based renewable energy systems, increasing attention has been paid to the power quality of power grids. Shunt active power filters (SAPFs) can efficiently solve the harmonic and reactive power compensation problems encountered in such grids. The control component of the SAPF determines the reference compensation current in real time and controls the power electronic devices to synthesize a compensation current [1]. In general, the compensation current can be generated using converters and filters. Amongst the various converters, three-level T-type converters ($3LT^2C$) have attracted considerable interest because of their excellent performance in terms of efficiency and controllability in low-voltage applications [2]–[4]. $3LT^2Cs$ offer many advantages, including lower output current ripples [5], [6] and higher overall efficiencies [7], [8]. In addition, to filter out the majority of high-order current harmonics, *LCL* filters have been widely used to sufficiently attenuate the harmonic current and comply with grid standards. The application of a $3LT^2C$ converter with an *LCL* filter can improve the quality of the SAPF compensation current and further reduce the total harmonic distortion (THD) of the grid current [9].

In recent years, the reliability of power converters has been widely studied [10]–[12]. One key measure for improving reliability is fault-tolerant control (FTC) [13], [14]. Moreover, for converter systems, the most likely faults relate to power-switching devices [15], for instance, short-circuit and open-circuit faults [16]. Short-circuit faults can cause serious damage to power devices and also affect other devices. Therefore, it is necessary to terminate the operation forcefully via the hardware devices. On the other hand, open-circuit faults can be caused by thermal cycling and gate-drive faults; these do not cause serious problems but make the compensation current of the SAPF

seriously inconsistent with its reference, which may worsen the compensation effect and lead to a neutral-point (NP) voltage fluctuation or imbalance [17]–[19].

Therefore, this article focuses on an FTC strategy for a 3LT^{2}C SAPF when an open-circuit fault occurs. In addition, the topology of the T-type converter indicates that its switching devices can be classified into horizontal NP switches and vertical half-bridge switches. The severity of the open-circuit faults in these two types of switches differs, as will be analyzed in this article.

The research into the FTC of SAPFs can be regarded as a category of FTC for converters because the output of the SAPF is a harmonic current, whereas ordinary converters directly output a fundamental current. In the literature, the FTC method for a SAPF is generally a redundancy device method [20], [21]. For example, Zhou and Tang [22] proposed an open-circuit fault diagnosis and tolerance scheme for a three-phase ac–dc converter, and they used model predictive control (MPC) to enhance its reliability; in this scheme, two new topologies were constructed by adding triacs and fuses on the bridge arms. Qunwei *et al.* [23] proposed a two-phase four-switch fault-tolerant strategy, in which a fourth bridge arm was included in the topology. In either case, redundant devices must be included in the existing SAPF topology to participate in the new control strategy in the event of an open-circuit fault. This is uneconomical and inefficient, owing to the need for additional components, such as insulated-gate bipolar transistors (IGBTs), fuses, and thyristors.

In fact, the fault-tolerance problems of power converters can be solved without adding any redundant devices; this is especially true of 3LT^{2}Cs. FTC strategies that only change the modulation algorithm have been widely described and studied [24], [25]. For example, the hybrid discontinuous switching tolerant control proposed in [26] maximally maintained a three-level modulation in sectors when an open-circuit fault occurred; however, the fluctuation of the NP voltage was not effectively inhibited. The hybrid switching tolerant control proposed in [27] considered the balance of the NP voltage during the modulation process. Because the output of the SAPF is harmonic and the reference vector of the converter output voltage fluctuates, it remains to be studied whether the aforementioned fault-tolerant strategies based on the modulation algorithm can be applied to SAPF.

To realize the FTC of the 3LT^{2}C SAPF, a novel control strategy is proposed here; it is referred to as sequential model predictive tolerant control (SMPTC). The idea of SMPTC is based on finite-control-set MPC (FCS-MPC), which has been a very popular prediction control method for power electronic systems in recent years [24], [27]. FCS-MPC predicts the state variables at future instances by modeling the discrete state-space equations of the system. Then, an optimization problem (cost function) is constructed to directly output the switching sequence required by the converter. Moreover, FCS-MPC itself also suffers from problems, including the selection of optimal weighting factors for the multiobjective cost function. For a multiobjective FCS-MPC design, the weighting factors are typically obtained by trial and error, which is time consuming [28], [29]. Sequential MPC (SMPC) can solve this problem well and has been studied by numerous scholars in motor control and other fields [30]–[32]. Under this method, the multiobjective optimization is transformed into several cascaded single-objective optimization problems. This idea is suitable for the FTC of the SAPF. The main contributions of this article are summarized as follows.

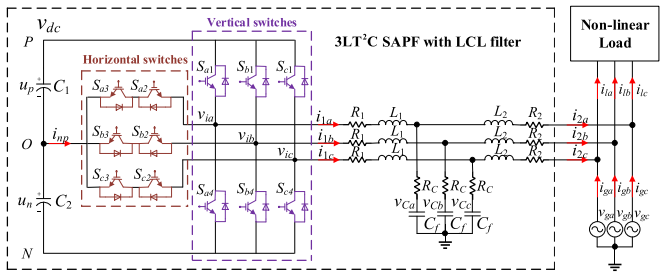

Fig. 1. Topology of the 3LT^{2}C SAPF with an *LCL* filter.

1) The similarities and differences between the horizontal NP and vertical half-bridge switch faults are analyzed; these can be used to evaluate the healthy and unhealthy states of the 3LT^{2}C SAPF.
2) An adaptive dc bus voltage regulation method is proposed, where the dc bus voltage of the 3LT^{2}C SAPF is automatically determined by the nonlinear load; this can avoid the time-consuming selection of the proper dc bus voltage for harmonic compensation.
3) A nonintegral lexicographic optimization SMPTC (LO-SMPTC) algorithm for resolving the multiobjective optimization problem (MOOP) is proposed to improve harmonic compensation and NP voltage balance under fault conditions.

The rest of this article is organized as follows. Section II presents an overview of the 3LT^{2}C SAPF, including the system configuration, space voltage vector diagram, harmonic extraction of the nonlinear load, and system prediction model. Section III presents the current path analysis used when an open-circuit fault occurs; furthermore, the evaluations of healthy and unhealthy 3LT^{2}Cs are also elaborated here. In Section IV, an adaptive dc bus voltage regulation control method for SAPF is proposed; this can prevent the improper setting of the dc bus voltage. Section V presents the improved SMPTC method. In Section VI, the experimental results under different scenarios are presented to validate the proposed method. Finally, Section VII concludes this article.

II. 3LT^{2}C SAPF With *LCL* Filter: An Overview

A. Configuration

Fig. 1 shows the topology of a 3LT^{2}C SAPF. The dc bus side consists of two series-connected capacitors C_1 and C_2, whose voltages are v_p and v_n, respectively. Because there is no dc power supply, the dc voltage $v_{\rm dc}$ is provided by the ac grid via an *LCL* filter. The 3LT^{2}C converter consists of six horizontal NP switches and six vertical half-bridge switches interfaced with an *LCL* filter; its parameters include the converter-side inductance L_1, grid-side inductance L_2, and filter capacitor C_f. R_1 and R_2

TABLE I
OUTPUT OF THE T-TYPE CONVERTER

Switching state	V_{out}	S_{i1}	S_{i2}	S_{i3}	S_{i4}
[P]	$0.5v_{dc}$	on	on	off	off
[O]	0	off	on	on	off
[N]	$-0.5v_{dc}$	off	off	on	on

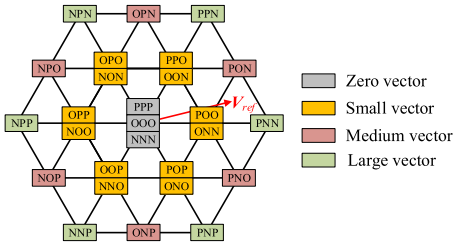

Fig. 2. Space voltage vector diagram for a 3LT^{2}C.

represent the parasitic resistances of L_1 and L_2, respectively, and R_C is the passive damping resistance. $i_{\rm np}$ is the NP current. v_i, i_1, i_2, v_C, i_g, v_g, and i_l are the converter-side voltage, converter-side current, SAPF output current, filter-capacitor voltage, grid current, grid voltage, and load current, respectively. The SAPF output i_2 compensates for the harmonic component of the load current i_l, thereby improving the quality of the grid current.

B. Space Voltage Vector of the 3LT^{2}C

According to the operational states of the four switching devices in each phase, the output voltage exhibits three voltage levels, as listed in Table I. Each phase of the 3LT^{2}C includes three switching states: [P], [O], and [N]. Thus, the 3LT^{2}C has 27 switching states, which can be interpreted as candidate voltage vectors (CVVs) for MPC.

These switching states can be represented by space voltage vectors, which are divided into four groups according to their magnitudes: 1) zero vector: $|\boldsymbol{V}_{\rm zero}| = 0$; 2) small vector: $|\boldsymbol{V}_{\rm small}| = v_{\rm dc}/3$; 3) medium vector: $|\boldsymbol{V}_{\rm medium}| = \sqrt{3}\, v_{\rm dc}/3$; and 4) large vector: $|\boldsymbol{V}_{\rm zero}| = 2v_{\rm dc}/3$.

The space voltage vectors of the 3LT^{2}C are shown in Fig. 2. The converter's modulation range is the tangent circle of a large hexagon with a radius of $\frac{\sqrt{3}}{3}v_{\rm dc}$. To prevent overmodulation, the magnitude reference of the converter-side voltage $|\boldsymbol{V}_{\rm ref}|$ should be smaller than this radius.

C. Harmonic Extraction

For the MPC of an SAPF, the harmonic current of the nonlinear load should be extracted and used as the reference for the cost function. The widely used i_p–i_q method was here adopted [33]–[35], as shown in Fig. 3. First, Clark and Park transformations were performed on the three-phase load currents. Because the phase-locked loop captures the phase of the grid voltage, the *d*-axis and *q*-axis denote the active and reactive components, respectively. Next, the load current components i_{ld} and i_{lq} were filtered via a low-pass filter with a 20-Hz cutoff frequency to remove the ac components. If the control requires the voltage and current of the grid to be in phase, the

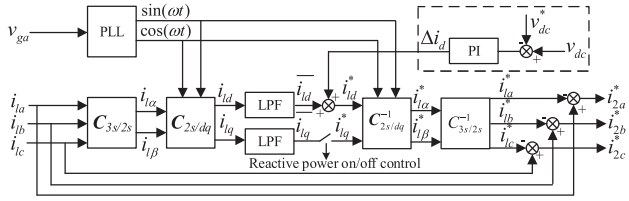

Fig. 3. Harmonic extraction diagram implementing i_p–i_q method.

reactive component is not required, and the switch in Fig. 3 can be disconnected. Finally, the fundamental component of the three-phase load current was obtained via the inverse Clark and Park transformations of the filtered current. The reference harmonic currents i_{2a}^*, i_{2b}^*, and i_{2c}^* are the results of the load currents minus the fundamental currents. Additionally, the dc bus voltage regulation block was constructed by introducing an active power reference signal Δi_d to the *d*-component.

D. Prediction Model of the 3LT^{2}C

Based on the requirements of FCS-MPC for discrete circuit equations, the *LCL* filter circuit was analyzed as follows: At any given instance, each CVV can be defined as

$$\begin{aligned} &\boldsymbol{u} = [u_a, u_b, u_c]^T \\ &\text{s.t. } u_a, u_b, u_c \in \{-1, 0, 1\} \boldsymbol{u} \in U \end{aligned} \tag{1}$$

where -1, 0, 1 represent [N], [O], and [P] states, respectively. U represents the finite control set of n CVVs.

Under the assumption of a balanced NP voltage, the converter-side voltage can be written as

$$\boldsymbol{v}_i = \frac{v_{\rm dc}}{2}\, \boldsymbol{u}. \tag{2}$$

According to Kirchhoff's law, and assuming that the three-phase circuit is symmetrical, the circuit equation for the *LCL* filter can be derived as

$$\begin{cases} \frac{d\boldsymbol{i}_1}{dt} = -\frac{R_C+R_1}{L_1}\boldsymbol{i}_1 + \frac{R_C}{L_1}\boldsymbol{i}_2 - \frac{1}{L_1}\boldsymbol{v}_C + \frac{\boldsymbol{v}_i}{L_1} \\ \frac{d\boldsymbol{i}_2}{dt} = \frac{R_C}{L_2}\boldsymbol{i}_1 - \frac{R_C+R_2}{L_2}\boldsymbol{i}_2 + \frac{1}{L_2}\boldsymbol{v}_C - \frac{1}{L_2}\boldsymbol{v}_g \\ \frac{d\boldsymbol{v}_C}{dt} = \frac{1}{C_f}\boldsymbol{i}_1 - \frac{1}{C_f}\boldsymbol{i}_2 \end{cases} \tag{3}$$

where $\boldsymbol{i}_1 = [i_{1a}, i_{1b}, i_{1c}]^T$ and the other bold vectors are written similarly to $\boldsymbol{i}_1$.

Setting the continuous-time state variable as $\boldsymbol{x}(t) = [\boldsymbol{i}_1(t), \boldsymbol{i}_2(t), \boldsymbol{v}_C(t)]^T$, we see that $\boldsymbol{x}(t)$ has nine variables. To reduce the number of state variables and simplify the calculations, the model can be transformed into $\alpha\beta$-stationary coordinates by Clark transformations, expressed as

$$\boldsymbol{C}_{3s/2s} = \frac{2}{3}\begin{bmatrix} 1 & -\frac{1}{2} & -\frac{1}{2} \\ 0 & \frac{\sqrt{3}}{2} & -\frac{\sqrt{3}}{2} \end{bmatrix}. \tag{4}$$

Thus, (3) can be rewritten as

$$\frac{d\boldsymbol{x}_{\alpha\beta}(t)}{dt} = \boldsymbol{F}\boldsymbol{x}_{\alpha\beta}(t) + \boldsymbol{G}\boldsymbol{u}(t) + \boldsymbol{P}\boldsymbol{v}_g(t) \tag{5}$$

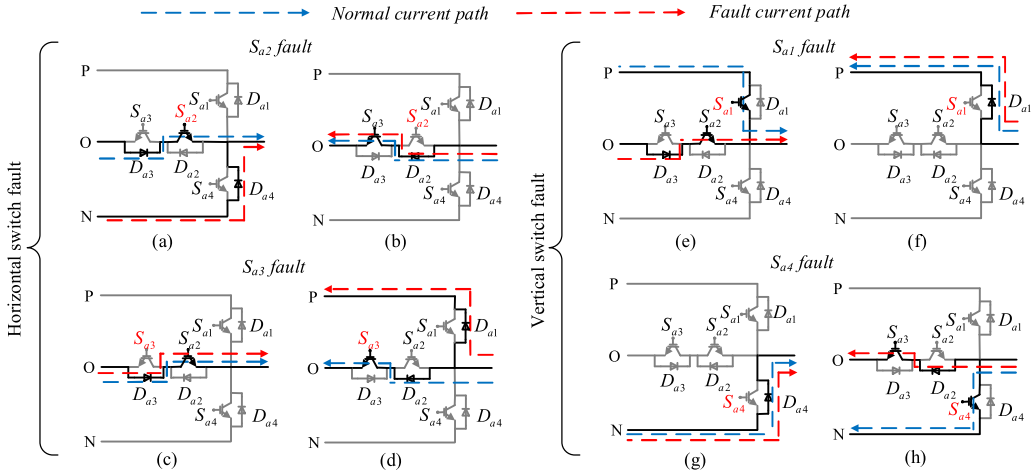

Fig. 4. Changes of the current paths under (a) $\boldsymbol{S_{a}2}$ fault, $\boldsymbol{i_{1a}} > 0$; (b) $\boldsymbol{S_{a}2}$ fault, $\boldsymbol{i_{1a}} < 0$; (c) $\boldsymbol{S_{a}3}$ fault, $\boldsymbol{i_{1a}} > 0$; (d) $\boldsymbol{S_{a}3}$ fault, $\boldsymbol{i_{1a}} < 0$; (e) $\boldsymbol{S_{a}1}$ fault, $\boldsymbol{i_{1a}} > 0$; (f) $\boldsymbol{S_{a}1}$ fault, $\boldsymbol{i_{1a}} < 0$; (g) $\boldsymbol{S_{a}4}$ fault, $\boldsymbol{i_{1a}} > 0$; and (h) $\boldsymbol{S_{a}4}$ fault, $\boldsymbol{i_{1a}} < 0$.

where $\boldsymbol{F} = \begin{bmatrix} -\frac{R_C+R_1}{L_1}\boldsymbol{I}_{2\times2} & \frac{R_C}{L_1}\boldsymbol{I}_{2\times2} & -\frac{1}{L_1}\boldsymbol{I}_{2\times2} \\ \frac{R_C}{L_2}\boldsymbol{I}_{2\times2} & -\frac{R_C+R_2}{L_2}\boldsymbol{I}_{2\times2} & \frac{1}{L_2}\boldsymbol{I}_{2\times2} \\ \frac{1}{C_f}\boldsymbol{I}_{2\times2} & -\frac{1}{C_f}\boldsymbol{I}_{2\times2} & \boldsymbol{O}_{2\times2} \end{bmatrix}$

$$\boldsymbol{G} = \begin{bmatrix} \frac{v_{dc}}{2L_1}\boldsymbol{I}_{2\times2} \\ \boldsymbol{O}_{2\times2} \\ \boldsymbol{O}_{2\times2} \end{bmatrix} \boldsymbol{C}_{3s/2s} \quad \boldsymbol{P} = \begin{bmatrix} \boldsymbol{O}_{2\times2} \\ -\frac{1}{L_2}\boldsymbol{I}_{2\times2} \\ \boldsymbol{O}_{2\times2} \end{bmatrix} \boldsymbol{C}_{3s/2s}.$$

By using the Du Hamel formula [36] to discretize (5), the discretized-time state-space equation can be obtained as

$$\boldsymbol{x}_{\alpha\beta}\,(k+1) = \boldsymbol{A}x_{\alpha\beta}(k) + \boldsymbol{B}u(k) + \boldsymbol{T}v_g(k) \tag{6}$$

where $\boldsymbol{A} = e^{\boldsymbol{F}T_s}, \boldsymbol{B} = -\boldsymbol{F}^{-1}(\boldsymbol{I}-\boldsymbol{A})\boldsymbol{G}, \boldsymbol{T} = -\boldsymbol{F}^{-1}(\boldsymbol{I}-\boldsymbol{A})\boldsymbol{P}$.

E. Prediction Model for NP Voltage

The NP voltage is an inherent problem in the three-level topology, that is, we must ensure that the two series-connected dc bus capacitors evenly divide the dc bus voltage. Let $C_1 = C_2$, then, according to the Kirchhoff current law, the current equations of node "O" can be derived as

$$\begin{aligned} i_{\rm np} &= (1-|u_a|)\ i_{1a} + (1-|u_b|)\,i_{1b} + (1-|u_c|)\,i_{1c} \\ &= C_1\,\frac{d(u_p-u_n)}{dt}. \end{aligned} \tag{7}$$

Equation (7) shows the relationship between the converter-side current and NP current. When a certain phase is in the [O] state, the NP current is equal to the converter-side current; when a certain phase is in the [P] or [N] state, the NP current is 0. Owing to the symmetry of the three phases, we have

$$i_{1a} + i_{1b} + i_{1c} = 0. \tag{8}$$

The NP voltage is defined as

$$u_{\rm np} = u_n - u_p. \tag{9}$$

Therefore, the NP current can be rewritten as

$$i_{\rm np} = -\left(|u_a|i_{1a} + |u_b|i_{1b} + |u_c|i_{1c}\right) = -C_1\frac{du_{\rm np}}{dt}. \tag{10}$$

TABLE II
SWITCHING STATE CHANGES UNDER A-PHASE SWITCH FAULT

Fault switch		i_{1a}	Normal switching state	Fault switching state
Horizontal switch	S_{a2}	+	[O]	[N]
		-	[O]	[O]
	S_{a3}	+	[O]	[O]
		-	[O]	[P]
Vertical switch	S_{a1}	+	[P]	[O]
		-	[P]	[P]
	S_{a4}	+	[N]	[N]
		-	[N]	[P]

By forward Euler discretization, the NP voltage [see (10)] in one switching period can be expressed as

$$u_{\rm np}\,(k+1) = \frac{T_s}{C_1}\,|\boldsymbol{u}(k)|^T\boldsymbol{i}_1\,(k) + u_{\rm np}\,(k) \tag{11}$$

where T_s represents the sampling interval.

III. Open-Circuit Fault Analysis of 3LT^{2}C SAPF

A. Current Path When Open-Circuit Fault Occurs

The fault of the switching device produces a change in the current path of the SAPF, which seriously reduces its compensation effect. Taking the A-phase as an example, the switch faults in the 3LT^{2}C can be classified into two categories: horizontal (S_{a2} and S_{a3}) and vertical (S_{a1} and S_{a4}). When a fault occurs, the switching state of the converter differs depending on the current direction and fault devices. Fig. 4 shows the current paths, where the dotted blue and red lines represent the current paths under normal and open-circuit fault conditions, respectively. The current flowing from the converter to the load is defined as the positive current. Because fault current analysis has been discussed in many previous studies [37]–[39], the conclusions are directly presented in Table II.

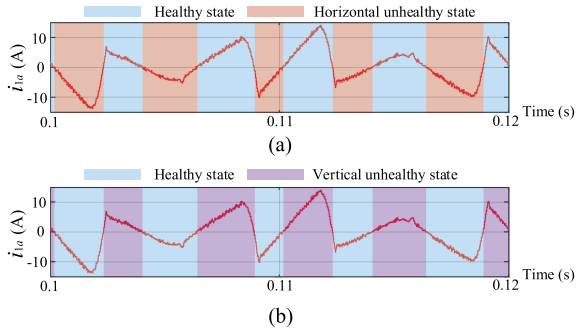

Fig. 5. Alternation between healthy and unhealthy states. (a) Horizontal $\boldsymbol{S_{a3}}$ fault. (b) Vertical $\boldsymbol{S_{a1}}$ fault.

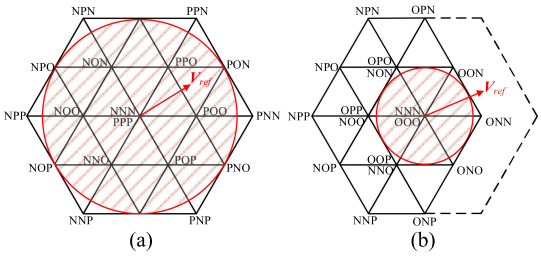

Fig. 6. Space voltage vector diagram of a 3LT^{2}C under. (a) Horizontal unhealthy state. (b) Vertical unhealthy state.

B. Healthy State Evaluation

Table II illustrates that fault switches can keep the switching state unchanged in a particular current direction; this does not reduce the control effect. Taking the fault of S_{a1} and S_{a3} as an example, we see that SAPF has three working states: 1) horizontal unhealthy state: S_{a3} fault and $i_{1a} < 0$; 2) vertical unhealthy state: S_{a1} fault and $i_{1a} > 0$; and 3) healthy state: all other conditions.

To demonstrate the diagnosis methods for the three working states more intuitively, Fig. 5 shows the diagnoses of the three working states after the application of the proposed fault-tolerant strategy. Fig. 5(a) represents the horizontal S_{a3} fault and (b) represents the vertical S_{a1} fault. In the case of a constant nonlinear load, each power frequency cycle (0.02 s) resembles that in Fig. 5, with alternating healthy and unhealthy states.

The biggest difference between these three working states is the difference in CVVs, which directly determines the maximum modulation range of the space vector diagram. The healthy state contains a total of 27 CVVs, and the spatial voltage vector diagram is shown in Fig. 2.

The space voltage vector diagram for the two unhealthy states is shown in Fig. 6. Because of the absence of [O] in Phase A, nine CVVs (OOO, OOP, OON, OPO, OPP, OPN, ONO, ONP, ONN) are missing in the horizontal unhealthy state. Nevertheless, because no large vectors are lost, the horizontal unhealthy state can still retain a double-hexagon structure similar to that in the healthy state; thus, the maximum modulation range is the inner tangent circle of the large hexagon with a radius of $\sqrt{3}v_{\rm dc}/3$.

Similarly, because of the absence of [P] in Phase A, nine CVVs (POO, POP, PON, PPO, PPP, PPN, PNO, PNP, PNN) are also unavailable in the vertical unhealthy state. The incomplete large hexagonal structure is caused by the absence of certain long vectors (PPN, PNN, PNP). Therefore, the maximum modulation range is reduced to the inner tangent circle of the small hexagon, with a radius of $\sqrt{3}v_{\rm dc}/6$.

The above analysis shows that faults in vertical switches are more serious than those in horizontal switches because the modulation radius is reduced by half. The solution to this problem is described in Section IV.

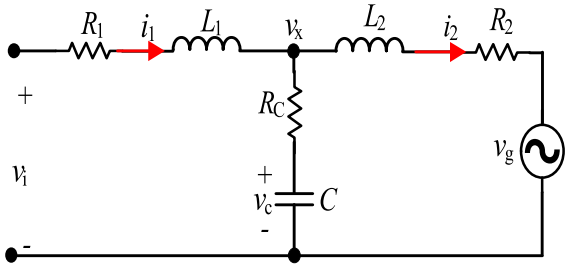

Fig. 7. Schematic diagram of an *LCL* filter circuit.

IV. Adaptive DC Bus Voltage Regulation

The modulation range of the SAPF varies sizably under different working states, and the modulation range is directly related to the dc bus voltage. In this chapter, an adaptive dc bus voltage control method is proposed to ensure that the reference voltage vector $\boldsymbol{V}_{\rm ref}$ does not exceed the modulation range in any working state.

A. Calculation of $v_{\rm dc}^*$

As shown in Fig. 3, a proportional–integral (PI) controller was adopted for dc bus voltage control in the outer loop. The time response for dc bus voltage control is much slower than the MPC-controlled output current in the inner loop, and this can avoid the interference between them. At the same time, if MPC is used to control the dc bus voltage, it will greatly complicate the control strategy and increase the calculation burden. Thus, a PI control was used instead of the MPC. As mentioned previously, the magnitude of the reference voltage vector should satisfy

$$\begin{cases} \text{Healthy state or horizontal unhealthy state} \\ |\boldsymbol{V}_{\rm ref}|_{\max} < \sqrt{3}v_{\rm dc}/3 \\ \text{Vertical unhealthy state}: |\boldsymbol{V}_{\rm ref}|_{\max} < \sqrt{3}v_{\rm dc}/6. \end{cases} \tag{12}$$

The harmonic component of the load current (i.e., the reference value of the SAPF output current i_2^*) is obtained from the harmonic extraction component in Fig. 3. Because the parameters of the filter circuit are fixed, $\boldsymbol{V}_{\rm ref}$ can be derived using phasor analysis.

The single-phase circuit of the *LCL* filter circuit is shown in Fig. 7. The SAPF output current i_{2a}^*, i_{2b}^*, and i_{2c}^* can be expressed in the phasor form $\boldsymbol{I}_2^*$ written as follows:

$$\left[\, i_{2\alpha}^* \;\; i_{2\beta}^* \,\right]^T = \boldsymbol{C}_{3s/2s}\left[\, i_{2a}^* \;\; i_{2b}^* \;\; i_{2c}^* \,\right]^T \tag{13}$$

$$\boldsymbol{I}_2^* = i_{2\alpha}^* + j * i_{2\beta}^*. \tag{14}$$

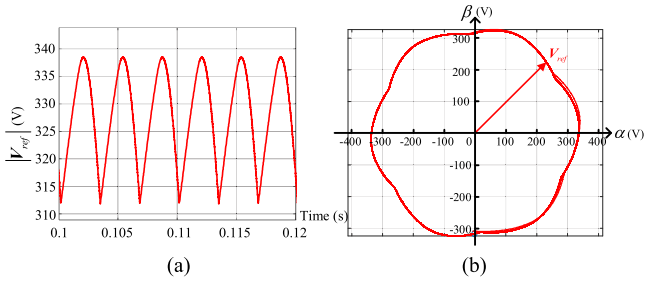

Fig. 8. Simulation results of converter-side voltage reference. (a) Variation of the magnitude. (b) Trajectory of the vector.

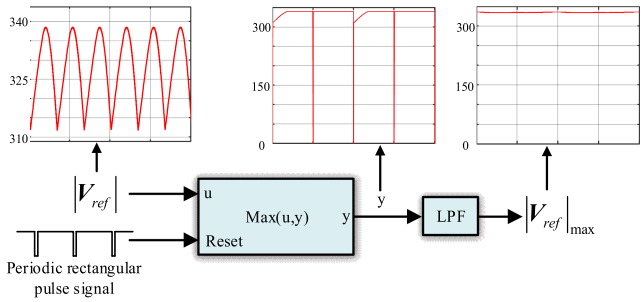

Fig. 9. Method of obtaining the maximum reference voltage vector.

Thus, the phasor analysis of Fig. 7 can be obtained as

$$\begin{cases} \boldsymbol{V}_x^* = \boldsymbol{V}_g + \boldsymbol{I}_2^*(R_2 + sL_2) \\ \boldsymbol{V}_C^* = \boldsymbol{V}_x^*/(1 + sC_f R_C) \\ \boldsymbol{I}_1^* = \boldsymbol{I}_2^* + sC_f \boldsymbol{V}_C^* \\ \boldsymbol{V}_{ref} = \boldsymbol{V}_x^* + \boldsymbol{I}_1^*(R_1 + sL_1) \end{cases} \tag{15}$$

where $s = j\omega$, and ω is the angular frequency of the grid.

Equation (15) ensures the real-time acquisition of $\boldsymbol{V}_{\mathrm{ref}}$. In this way, the reference dc bus voltage v_{dc}^* under different working states can be determined and written as

$$\begin{cases} \text{Healthy state or horizontal unhealthy state} \\ : v_{\mathrm{dc}}^* = \sqrt{3}k_1 |\boldsymbol{V}_{\mathrm{ref}}|_{\max} \\ \text{When a vertical unhealthy state occurs} \\ : v_{\mathrm{dc}}^* = 2\sqrt{3}k_2 |\boldsymbol{V}_{\mathrm{ref}}|_{\max} \end{cases} \tag{16}$$

where k_1 and k_2 are the margin coefficients.

B. Maximum Magnitude Calculation of $\boldsymbol{V}_{\mathrm{ref}}$

The SAPF outputs the harmonic current and its vector magnitude fluctuates. Therefore, the magnitude of $\boldsymbol{V}_{\mathrm{ref}}$ obtained using (15) may vary. To clarify this phenomenon more clearly, Fig. 8 depicts the magnitude variation and vector-space trajectory of $\boldsymbol{V}_{\mathrm{ref}}$.

Fig. 8 shows that $|\boldsymbol{V}_{\mathrm{ref}}|$ changes periodically when SAPF is in steady state. To ensure that $\boldsymbol{V}_{\mathrm{ref}}$ stays within the modulation range at any time, its maximum value must be periodically obtained. Fig. 9 illustrates a simple approach. A $\mathrm{Max(u, y)}$ function is proposed to obtain the maximum $|\boldsymbol{V}_{\mathrm{ref}}|$ with a period of 5 ms. A periodic rectangular pulse signal resets the function, and the ratio of the pulse is 1%. The output y is 0 when the function is reset, which causes periodical concave spikes in y. When y is low-pass filtered, the maximal $|\boldsymbol{V}_{\mathrm{ref}}|$ can be obtained. Although the waveform fluctuates a little, it meets the requirement of adaptive dc bus voltage control. For example, when SAPF changes from the healthy state to vertical unhealthy state, $|\boldsymbol{V}_{\mathrm{ref}}|_{\max}$ is calculated in real time through the above method; then, v_{dc}^* is calculated using (16). Finally, the PI adjustment in Fig. 3 ensures that v_{dc} can track the reference value. It is not necessary to preset any parameters, except for the proportional and integral coefficients of the PI controller.

V. FTC With Multiobjective Optimization Under Open-Circuit Fault

A. Control Objectives

The 3LT^{2}C SAPF has two control objectives. One is the accurate and fast tracking of the output reference current $\boldsymbol{i}_2^*(k)$; the other is the balance of the NP voltage.

1) Reference Current Tracking of SAPF: The filter circuit predictive relationship described in (6) includes three control variables: the converter-side current i_1, filter capacitor voltage v_C, and SAPF output current i_2. Note that passive damping is applied to the *LCL* filter for resonance damping in this article; therefore, the control for i_1 and v_C is unnecessary. Thus, by defining the output variable $\boldsymbol{y}(k+1)$, the relationship between $\boldsymbol{y}(k+1)$ and state variable $\boldsymbol{x}_{\alpha\beta}(k+1)$ can be written as

$$\boldsymbol{y}\ (k+1) = [00, i_{2\alpha}(k+1), i_{2\beta}(k+1), 00]^T = \boldsymbol{C}\boldsymbol{x}_{\alpha\beta}(k+1) \tag{17}$$

where $\boldsymbol{C} = \mathrm{diag}(00, 11, 00)$.

It is important to note here that although the control for i_1 and v_C can be neglected in (17), the sampling cannot be ignored. This is because the prediction model [(6)] requires the sampling of all state variables. Therefore, to reduce the number of sensors, a Kalman filter (KF) [40] was used to estimate the converter-side current $\boldsymbol{i}_1$ and filter capacitor voltage $\boldsymbol{v}_C$. The reference values of $\boldsymbol{i}_2$ were derived from the harmonic extraction component of Fig. 3. To obtain the predicted reference current, Lagrange extrapolation with two-step prediction can be applied and expressed as follows:

$$\boldsymbol{i}_2^*(k+1) = 3\boldsymbol{i}_2^*(k) - 3\boldsymbol{i}_2^*(k-1) + \boldsymbol{i}_2^*(k-2). \tag{18}$$

After transforming $\boldsymbol{i}_2^*(k+1)$ into two stationary coordinates, the predicted state variable reference of the SAPF is

$$\boldsymbol{y}^*(k+1) = [0, 0, \boldsymbol{i}_{2\alpha}^*(k+1), \boldsymbol{i}_{2\beta}^*(k+1), 0, 0]^T. \tag{19}$$

According to the above analysis, the cost function for the current grid current tracking can be written as

$$\begin{aligned} J_t &= \|\boldsymbol{y}(k+1) - \boldsymbol{y}^*(k+1)\| \\ &= \|\boldsymbol{C}(\boldsymbol{A}\boldsymbol{x}_{\alpha\beta}(k) + \boldsymbol{B}\boldsymbol{u}(k) + \boldsymbol{T}\boldsymbol{v}_g(k)) - \boldsymbol{y}^*(k+1))\| \end{aligned} \tag{20}$$

where $\|\cdot\|$ represents the two-norm of a vector.

2) Balance of NP Voltage: The predictive NP voltage relationship derived from (11) can be directly used in the cost function. To balance the NP voltage, the reference value of u_{np} should be set to 0. Therefore, the cost function of the NP voltage

can be written as

$$J_{\rm np} = |u_{\rm np}(k+1) - 0| = \left| \frac{T_s}{C_1} |\boldsymbol{u}(k)|^T \boldsymbol{i}_1(k) + u_{\rm np}(k) \right|. \tag{21}$$

B. Lexicographic Method for MOOP

The two cost functions J_t and $J_{\rm np}$ constitute the MOOP. To solve the MOOP, the traditional MPC (t-MPC) combines multiple cost functions with weighting factors, and the optimal solution can be expressed as

$$\begin{aligned} &\boldsymbol{u}_{\rm opt}(k) = \arg\min_{\boldsymbol{u}(k)} \sum_{i=1}^{p} \lambda_i J_i(\boldsymbol{u}(k), \boldsymbol{x}_i(k)) \\ &\text{s.t. } \boldsymbol{u}(k) \in U \text{card}(U) = n, \end{aligned} \tag{22}$$

where p represents the number of cost functions, $\boldsymbol{x}$ represents the control objective, λ represents the weighting number, and U represents the set of n CVVs. The cost function $J_{\rm t-MPC}$ for the 3LT^{2}C SAPF is designed as

$$\begin{aligned} J_{t-\rm MPC} &= J_t + J_{\rm np} \\ &= \|\boldsymbol{C}(\boldsymbol{A}\boldsymbol{x}_{\alpha\beta}(k) + \boldsymbol{B}\boldsymbol{u}(k) + \boldsymbol{T}\boldsymbol{v}_g(k)) - \boldsymbol{y}^*(k+1))\| \\ &\quad + \lambda_{\rm np} \left| \frac{T_s}{C_1} |\boldsymbol{u}(k)|^T \boldsymbol{i}_1(k) + u_{\rm np}(k) \right| \end{aligned} \tag{23}$$

where $\lambda_{\rm np}$ is the weighting factor. The quantitative relationship between different cost functions is unclear, indicating that trial and error is necessary for selecting the optimal weighting factor.

To solve the MOOP without weighting factors, it is necessary to simultaneously minimize p different cost functions. An effective method for these solutions is the lexicographic optimal solution. The lexicographic method for MOOPs is described as follows. The first layer is the most important objective, whereas the last one has the lowest priority. Then, each objective is minimized sequentially using additional constraints, which guarantees that the previous objectives generate optimal values. To ensure multiple solutions for all layers except the last, suboptimal solutions can also be applied. Algorithm 1 illustrates this control strategy, referred to as the SMPC.

In Algorithm 1, "sort ()" is a function that sorts the cost function vectors from smallest to largest. In this way, n_{i+1} suboptimal solutions (including the optimal solution) can be selected for layer i, and n_i are reduced layerwise. The last layer yields a unique optimal solution $\boldsymbol{u}_{\rm opt}(k)$. The two control objectives required to control the 3LT^{2}C SAPF were identified; thus, the control flow of the SMPC was straightforward. However, limitations remain in the following processes.

1) First, the method of determining the priority of the two control objectives: current reference tracking and NP voltage balance.
2) Second, the method of determining the number of suboptimal solutions selected by the first layer, especially under large numbers of CVVs in the 3LT^{2}C.

Algorithm 1: Obtain The Optimal Solution of MOOP Via SMPC.

s.t. $\boldsymbol{u}(k) \in U_1, \text{card}(U_1) = n_1$
$\forall\, \text{i} = 1, \ldots, \text{p} - 1, n_i > n_{i+1}, n_p \geq 2$
Prioritize $J_1 \rightarrow \ldots \rightarrow J_p$
for $m = 1, \ldots, n_1$ **do**
  $J_1^m = J_1(\boldsymbol{u}^m(k), \boldsymbol{x}_1(k))$
end for
  $\boldsymbol{J}_1 = [J_1^1, \ldots, J_1^{n_1}]^T$
  $\boldsymbol{array}_1 = \text{sort}(\boldsymbol{J}_1)$
for $i = 2, \ldots, p-1$ **do**
  for $m = 1, \ldots, n_i$ **do**
    $J_i^m = J_i(\boldsymbol{u}^{\boldsymbol{array}_{i-1}^m}(k), \boldsymbol{x}_i(k))$
  end for
  $\boldsymbol{J}_i = [J_i^1, \ldots, J_i^{n_i}]^T$
  $\boldsymbol{array}_i = \text{sort}(\boldsymbol{J}_i)$
end for
  $\boldsymbol{u}_{opt}(k) = \underset{\boldsymbol{u}(k)}{\text{argmin}}\{J_p(\boldsymbol{u}^{\boldsymbol{array}_{p-1}^m}(k), \boldsymbol{x}_p(k)) | m = 1, \ldots, n_p\}$

C. LOSMPC for 3LT^{2}C SAPF

As mentioned above, when SMPC deals with three-level problems (e.g., the weighting factor of t-MPC), it must also artificially select the number of first-level suboptimal solutions. This parameter is defined as the weighting number n_2. The 3LT^{2}C SAPF has 18 CVVs (nine missing) in an unhealthy state and 27 CVVs in a healthy one. The difficulty in choosing the weighting number is significantly increased compared to the two-level SAPF with only eight CVVs.

Nevertheless, the problem can be solved using the cost function of the NP voltage balance [see (21)]. From (21), switching states 1 and -1 in $\boldsymbol{u}(k)$ can be seen to have the same effect on the cost function result because $\boldsymbol{u}(k)$ has an absolute value sign. Therefore, $|\boldsymbol{u}(k)|$ was selected as the independent variable for the cost function $J_{\rm np}$. Table III lists all cases of $|\boldsymbol{u}(k)|$ under the three working states. As shown, the CVVs are reduced to eight in the healthy and vertical unhealthy states and only four in the horizontal unhealthy state. The cost function of the reference current tracking J_t offers none of the above advantages because $\boldsymbol{u}(k)$ has no absolute value sign; this brings us to the priority determination problem.

From the control priority perspective, it seems that J_t would be the highest priority, followed by $J_{\rm np}$. This is impractical because J_t has too many CVVs and cannot reduce them using the absolute value sign in $J_{\rm np}$. Based on the above analysis, $J_{\rm np}$ is mandated to have the highest priority. After n_2 suboptimal solutions are obtained, Table III is used to remove the absolute values, and the integrated CVV set is used to calculate the optimal solution of J_t.

Compared with SMPC and t-MPC, it is very convenient to select the weighting number n_2; however, there is still room for simplification. For example, in a healthy state, $J_{\rm np}$ would have eight values with different distributions at each sampling time, as shown in Fig. 10. The cost functions are arranged in

TABLE III
CVVs OF $|\boldsymbol{u}(k)|$ AND CORRESPONDING VOLTAGE VECTORS OF $\boldsymbol{u}(k)$ IN DIFFERENT WORKING STATES

Working state	CVVs of $\lvert\boldsymbol{u}(k)\rvert$ / Corresponding voltage vectors of $\boldsymbol{u}(k)$							
Healthy state	OOO	OOP	OPO	OPP	POO	POP	PPO	PPP
	OOO	OOP, OON	OPO, ONO	OPP, OPN, ONP, ONN	POO, NOO	POP, PON, NOP, NON	PPO, PNO, NPO, NNO	PPP, PPN, PNP, PNN, NPP, NPN, NNP, NNN
Horizontal unhealthy state	POO		POP		PPO		PPP	
	POO, NOO		POP, PON, NOP, NON		PPO, PNO, NPO, NNO		PPP, PPN, PNP, PNN, NPP, NPN, NNP, NNN	
Vertical unhealthy state	OOO	OOP	OPO	OPP	POO	POP	PPO	PPP
	OOO	OOP, OON	OPO, ONO	OPP, OPN, ONP, ONN	NOO	NOP, NON	NPO, NNP	NPP, NPN, NNP, NNN

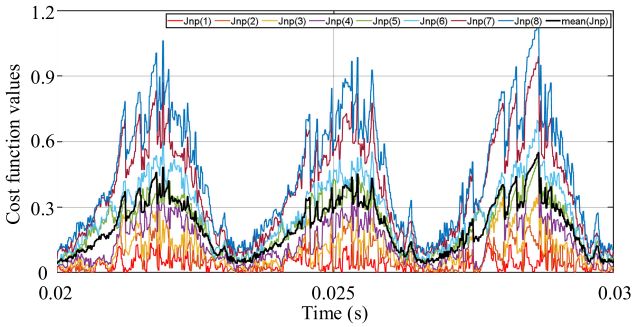

Fig. 10. Cost function distributions and mean values.

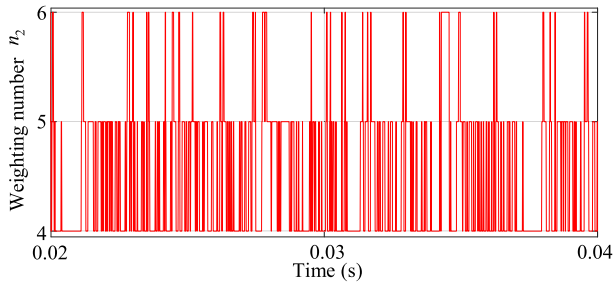

Fig. 11. Simulation results of weighting number.

ascending order at each sampling, and no lines correspond to a specific CVV. To avoid the selection of any parameter in SMPC, the mean value of all cost function values can be calculated (bold black line in Fig. 10), and n_2 is defined as the cost function below the mean value, namely

$$n_2 = \mathrm{Card}\left\{ J_{\mathrm{np}}^m \middle| J_{\mathrm{np}}^m < \left(\sum_{m=1}^{n_1} {J_{\mathrm{np}}}^m \right) / n_1 \right\} \tag{24}$$

where

$$n_1 = \begin{cases} 4, \text{Horizontal unhealthy state} \\ 8, \text{Healthy state or vertical unhealthy state.} \end{cases}$$

The n_2 calculated by (24) is not constant because the above method is based on the mean rather than the median. As shown in Fig. 11, n_2 is selected differently in real time using the above method such that the number of CVVs has different probability distributions. Fig. 11 shows that, in the period 0.02–0.04 s, the probability of n_2 being equal to 4, 5, and 6 are 42.72%, 45.89%, and 11.39%. n_2 has a mathematical expectation of 4.69, that is, J_{np} can compute noninteger suboptimal solutions at the macroscale more flexibly than the SMPC.

Algorithm 2: Fault-Tolerant LOSMPC Method.

s.t. $\boldsymbol{u}(k) \in U_1$, card $(U_1) = n_1$
sample/calculate variables and references
for $m = 1, \ldots, n_1$ **do**
  $J_{\mathrm{np}}^m = J_{\mathrm{np}}\ (|\boldsymbol{u}(k)|^m)$
end for
  $\boldsymbol{J}_1 = [J_{\mathrm{np}}^1, \ldots, J_{\mathrm{np}}^{n_1}]^T$
  $\boldsymbol{array}_{\mathrm{np}} = \mathrm{sort}(\boldsymbol{J}_{\mathrm{np}})$
  $n_2 = \mathrm{card}\{J_{\mathrm{np}}^m | J_{\mathrm{np}}^m < (\sum_{m=1}^{n_1} J_{\mathrm{np}}^m)/n_1\}$
  $U_2 = \varnothing$
for $m = 1, \ldots, n_2$ **do**
  $|\boldsymbol{u}(k)|^{\boldsymbol{array}_{\mathrm{np}}^m} \overset{\text{Table III}}{\rightarrow} U_{\mathrm{track}}^m$
  $U_2 = U_2 \cup U_{\mathrm{track}}^m$
end for
  $\boldsymbol{u}_{\mathrm{opt}}\ (k) = \underset{\boldsymbol{u}(k)}{\mathrm{argmin}}\{J_{\mathrm{track}}(\boldsymbol{u}(k)) | \boldsymbol{u}(k) \in U_2\}$

Based on the above analysis, Algorithm 2 displays the implementation of the LOSMPC to tackle the fault-tolerance problem of the 3LT^{2}C SAPF. The selection of CVV set U_1 varies according to the three working states (i.e., all the situations corresponding to $|\boldsymbol{u}(k)|$ in Table III). After selecting the suboptimal solutions of J_{np}, they remove the absolute value according to Table III and integrate into the CVV set U_2 for J_t.

Without the loss of generality, Algorithm 3 shows the process of the lexicographic optimization SMPC (LOSMPC) for general MOOPs. In choosing the weighting numbers, other values (e.g., the geometric mean) can also be used instead of the arithmetic mean; however, the influence on the control effect remains to be studied.

D. Stability Analysis

Assume that the state-space model of 3LT^{2}C SAPF, when considering the model uncertainty, is

$$\begin{cases} x\ (k+1) = \ Ax(k) + Bu(k) + Td(k) \\ \mathbf{y_c}\ (k) = \boldsymbol{\lambda_c}\ x(k) \end{cases} \tag{25}$$

where $\boldsymbol{x}(k) \in \mathbb{R}^{n_x}$ is the state variable, $\boldsymbol{u}(k) \in \mathbb{R}^{n_u}$ is the input control variable, $\boldsymbol{y_c}(k) \in \mathbb{R}^{n_c}$ is the output control variable, and

Algorithm 3: Obtain the Optimal Solution for MOOP Via LOSMPC.

s.t. $\boldsymbol{u}(k) \in U_1$, card $(U_1) = n_1$
$\forall$ i $= 1, \ldots,$ p $- 1, n_i > n_{i+1}, n_p \geq 2$
Prioritize $J_1 \rightarrow \ldots \rightarrow J_p$
for $m = 1, \ldots, n_1$ **do**
$J_1^m = J_1\ (\boldsymbol{u}^m(k), \boldsymbol{x}_1(k))$
end for
$\boldsymbol{J}_1 = [J_1^1, \ldots, J_1^{n_1}]^T$
$\boldsymbol{array}_1 =$ sort$(\boldsymbol{J}_1)$
$n_2 =$ card$\{J_1^m | J_1^m < (\sum_{m=1}^{n_1} J_1^m)/n_1\}$
for $i = 2, \ldots, p-1$ **do**
for $m = 1, \ldots, n_i$ **do**
$J_i^m = J_i\ (\boldsymbol{u}^{\boldsymbol{array}_{i-1}^m}(k), \boldsymbol{x}_i(k))$
end for
$\boldsymbol{J}_i = [J_i^1, \ldots, J_i^{n_i}]^T$
$\boldsymbol{array}_i =$ sort$(\boldsymbol{J}_i)$
$n_{i+1} =$ card$\{J_i^m | J_i^m < (\sum_{m=1}^{n_i} J_i^m)/n_i\}$
end for
$\boldsymbol{u}_{opt}\ (k) = \underset{\boldsymbol{u}(k)}{\text{argmin}}\{J_p(\boldsymbol{u}^{\boldsymbol{array}_{p-1}^m}(k), \boldsymbol{x}_p(k)) | m = 1, \ldots, n_p\}$

$\boldsymbol{d}(k)$ is the disturbance. Note that the grid voltage is considered as the disturbance.

To reduce the steady-state error, we can rewrite the system in (25) as an incremental model as

$$\Delta \boldsymbol{x}\ (k+1) = \mathbf{A}\Delta \boldsymbol{x}(k) + \boldsymbol{B}\Delta \boldsymbol{u}(k) + \boldsymbol{T}\Delta \boldsymbol{d}(k) \tag{26}$$

where $\Delta x\ (k) = x(k) - x(k-1)$, $\Delta u\ (k) = u(k) - u(k-1)$, and $\Delta d\ (k) = d(k) - d(k-1)$.

Thus, the system prediction error at instant $k+1$ can be expressed as

$$\boldsymbol{E}_P\ (k+1|k) = \boldsymbol{R}(k+1) - \boldsymbol{Y}(k+1) \quad = \boldsymbol{R}(k+1) - \boldsymbol{S}_x \Delta x(k) - \boldsymbol{\gimel}\mathbf{y_c}(k) - \boldsymbol{S_d}\Delta d(k) - \boldsymbol{S_u}\Delta \boldsymbol{u}(k) \tag{27}$$

where

$$\boldsymbol{S}_x = [\boldsymbol{\lambda A}\ \boldsymbol{\lambda A}^2\ \boldsymbol{\lambda A}^3 \ldots\ \boldsymbol{\lambda A}^N]^T$$

$$\boldsymbol{\gimel} = [\boldsymbol{I}_{nc\times nc}\ \boldsymbol{I}_{nc\times nc}\ \ldots\ \boldsymbol{I}_{nc\times nc}]^T$$

$$\boldsymbol{S_d} = \begin{bmatrix} \boldsymbol{\lambda B} & 0 & \cdots & 0 \\ \boldsymbol{\lambda AB} & \boldsymbol{\lambda B} & \cdots & 0 \\ \vdots & \vdots & \ddots & \vdots \\ \boldsymbol{\lambda A}^{N-1}\boldsymbol{B} & \boldsymbol{\lambda A}^{N-2}\boldsymbol{B} & \cdots & \boldsymbol{\lambda B} \end{bmatrix}$$

$$\boldsymbol{S_u} = \begin{bmatrix} \boldsymbol{\lambda T} & 0 & \cdots & 0 \\ \boldsymbol{\lambda AT} & \boldsymbol{\lambda T} & \cdots & 0 \\ \vdots & \vdots & \ddots & \vdots \\ \boldsymbol{\lambda A}^{N-1}\boldsymbol{T} & \boldsymbol{\lambda A}^{N-2}\boldsymbol{T} & \cdots & \boldsymbol{\lambda T} \end{bmatrix}.$$

Based on the principle of MPC, only the first element of the open-loop optimal control sequence acts on the T-type converter; that is

$$\Delta \boldsymbol{u}\ = \left[\boldsymbol{I}_{nc\times nc}\ 0 \cdots 0\right]\ \Delta \boldsymbol{U}^*\ (k) \tag{28}$$

where $\Delta \boldsymbol{U}^*$ is the optimal control sequence expressed as

$$\Delta \boldsymbol{U}^*\ (k) = (\boldsymbol{S}_u^T \boldsymbol{\Gamma}_y^T \boldsymbol{\Gamma}_y \boldsymbol{S}_u + \boldsymbol{\Gamma}_u^T \boldsymbol{\Gamma}_u)^{-1}\ \boldsymbol{S}_u^T \boldsymbol{\Gamma}_y^T \boldsymbol{E}_P(k+1|k). \tag{29}$$

Defining the control gain $\boldsymbol{K}_{\text{mpc}}$ of the prediction controller as

$$\boldsymbol{K}_{\text{mpc}} = \left[\boldsymbol{I}_{nc\times nc}\ 0 \cdots 0\right]_{1\times m} (\boldsymbol{S}_u^T \boldsymbol{\Gamma}_y^T \boldsymbol{\Gamma}_y \boldsymbol{S}_u + \boldsymbol{\Gamma}_u^T \Gamma_u)^{-1} \boldsymbol{S}_u^T \boldsymbol{\Gamma}_y^T \boldsymbol{E}_P\ (k+1|k) \tag{30}$$

$\Delta \boldsymbol{u}(k)$ can be derived using (29) and (30) as

$$\begin{aligned} \Delta \boldsymbol{u}\ (k) &= \boldsymbol{K}_{\text{mpc}}\ \boldsymbol{E}_P(k+1|k) \\ &= \boldsymbol{K}_{\text{mpc}}\ (\boldsymbol{R}(k+1) \\ &- \boldsymbol{S}_x \Delta \boldsymbol{x}(k) - \boldsymbol{\gimel \lambda_c x}(k)\ - \boldsymbol{S_d}\Delta \boldsymbol{d} = (k)\boldsymbol{K}_{\text{mpc}}\ \boldsymbol{R}(k+1) \\ &- \boldsymbol{K}_{\text{mpc}}(\boldsymbol{S_x} + \boldsymbol{\gimel \lambda_c})\Delta \boldsymbol{x}(k) - \boldsymbol{K}_{\text{mpc}}\boldsymbol{\gimel \lambda}_c x(k-1) \\ &- \boldsymbol{K}_{\text{mpc}}\ \boldsymbol{S}_d \Delta d(k). \end{aligned} \tag{31}$$

Thus, the closed-loop system can be expressed as

$$\begin{aligned} \Delta \boldsymbol{x}\ (k+1) &= (\boldsymbol{A} - \boldsymbol{BK_{mpc}}(\boldsymbol{S}_x + \boldsymbol{\gimel \lambda}_c))\ \Delta \boldsymbol{x}(k) \\ &+ \boldsymbol{BK}_{\text{mpc}}\boldsymbol{R}(k+1) + (\boldsymbol{T} - \boldsymbol{BK}_{\text{mpc}}S_d) \\ &\Delta \boldsymbol{d}(k) - \boldsymbol{BK}_{mpc}\boldsymbol{\gimel \lambda}_c \boldsymbol{x}(k-1). \end{aligned} \tag{32}$$

Therefore, when all the characteristic roots of the matrix $\boldsymbol{A} - \boldsymbol{BK}_{\text{mpc}}(\boldsymbol{S_x} + \boldsymbol{\gimel \lambda_c})$ are located within the unit circle, the closed-loop control system is stable. For an *LCL*-interfaced 3LT^{2}C SAPF, $\boldsymbol{K}_{\text{mpc}}$ is the optimal switching sequence to minimize the cost function; this should satisfy $|\boldsymbol{A} - \boldsymbol{BK}_{\text{mpc}}(\boldsymbol{S_x} + \boldsymbol{\gimel \lambda_c})| < 1$. Thus, for the MPC control problem without constraints, the calculated $\boldsymbol{K}_{\text{mpc}}$ should be substituted into the characteristic roots of the matrix.

E. Block Diagram of the Proposed LOSMPTC Method

The control block diagram of the proposed FTC strategy is shown in Fig. 12. This strategy systematically constructs the integrated control method of 3LT^{2}C SAPF under open-switch faults (S_{a3} and S_{a1} open-switch faults represent the horizontal and vertical switch faults, respectively) and normal operation.

The overall control system is primarily divided into the following three components.

1) Determination of working state: Distinguishing the three different working states ensures that the two remaining control parts can be adjusted automatically in real time. Note that the fault diagnosis method was not studied here. In the experiment, trigger signals were used to determine the three working states.
2) Adaptive dc bus voltage control: As mentioned above, the reference value of the dc bus voltage can be adjusted adaptively according to the working state. The output of the PI regulator was input to the harmonic extraction module, and the adjusted current reference value was sent to the MPC to form a closed control loop.
3) Fault-tolerance LOSMPC. The NP voltage was controlled first, the reference current tracking was controlled second,

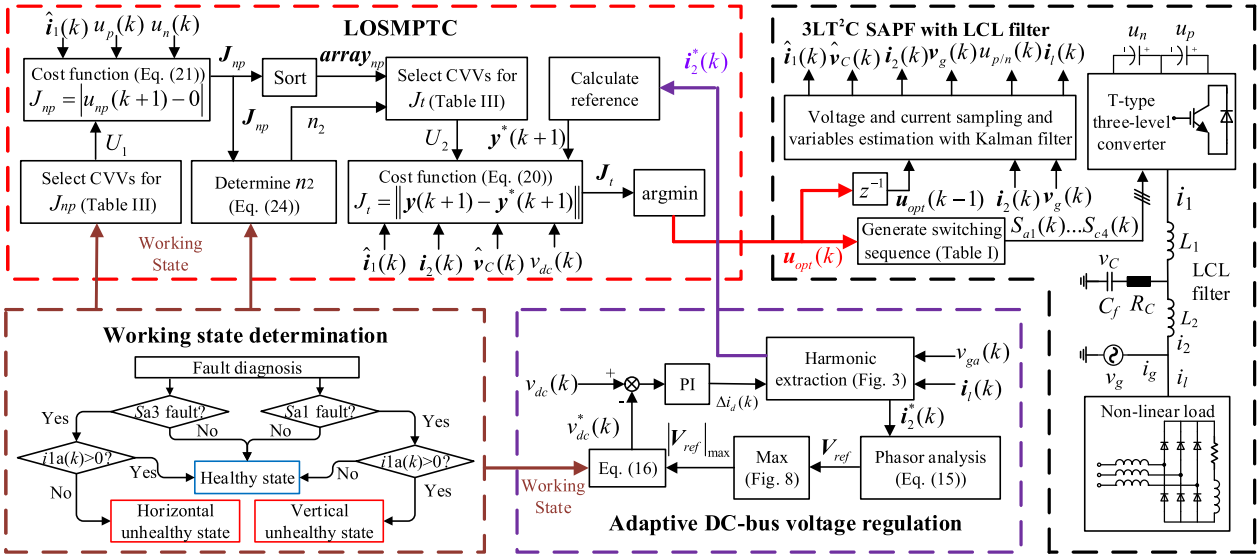

Fig. 12. Proposed FTC block diagram for the 3LT^{2}C SAPF.

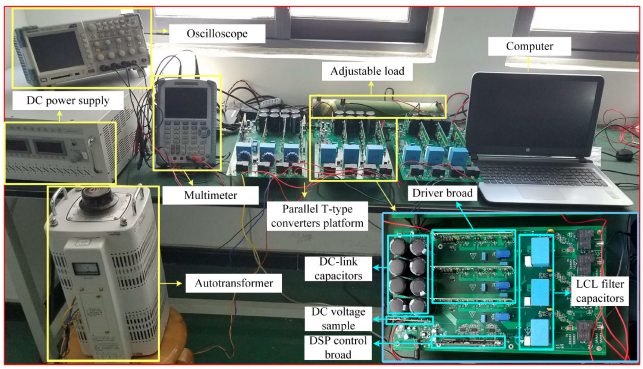

Fig. 13. Schematic diagram of the experimental setup.

TABLE IV
EXPERIMENTAL PARAMETER SPECIFICATIONS

Parameter	Description	Values
C_1 (μF)	DC-link capacitance	500
L_1 (mH)	Converter-side inductance	6
L_2 (μH)	Grid-side inductance	10
C (μF)	Filter capacitance	10
R_1 (Ω)	Converter-side resistance	0.1
R_2 (Ω)	Grid-side resistance	0.1
R_c (Ω)	Resonance damping resistance	2
V_g (V)	Grid voltage (RMS)	$220\sqrt{2}$
ω (rad/s)	Grid frequency	314.16
f_s (kHz)	Sampling frequency	50
K_p	Proportion coefficient	0.05
K_i	Integral coefficient	0.2
k_1	Margin coefficient 1	1.3
k_2	Margin coefficient 2	1.2

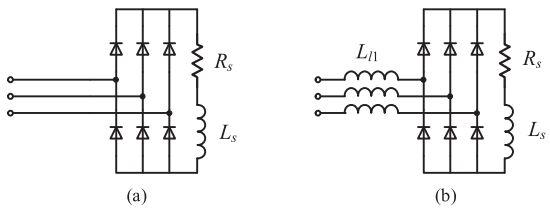

Fig. 14. Two kinds of nonlinear loads. (a) Without L_{i1}. (b) With L_{i1}.

and the weighting number between the two was nonarbitrarily selected. Under different working states, the CVVs selected using Table III and the current reference ensured a sufficient modulation range and optimal control effect.

VI. EXPERIMENTAL RESULTS

A. Hardware Setup

To verify the effectiveness of the proposed strategy, a three-phase 3LT^{2}C LCL-type SAPF with a rated power of 10 kW was built in the laboratory. Fig. 13 shows the experimental setup, in which the SMPTC control algorithm was realized by a 32-bit floating-point digital signal processor TMS320F28379 (Texas Instrument Company, USA), which is usually used for fast and complex digital calculations and control algorithm implementation. The 3LT^{2}C consists of six FUZI 1MBH50D-060 IGBTs and six FUZI 2MBI150U2A-060 IGBTs. Six Hall current sensors (HCS-LTS-06A) were used to measure the converter current and grid current. A fundamental frequency transformer was applied for voltage matching between the converter and grid voltages. The specific parameters of the control system are listed in Table IV.

B. Trouble-Free Steady-State Experiments

1) Nonlinear Load Analysis: In engineering, it is generally impossible to know the specific circuit of a nonlinear load: we can only obtain its current. However, in the literature, two typical circuit topologies are commonly used as nonlinear loads, as shown in Fig. 14. The experimental parameters are listed in Table V. Clearly, the biggest difference between the two

TABLE V
EXPERIMENTAL PARAMETER OF NONLINEAR LOAD

Parameter	Description	Values
L_{l1} (mH)	Current-limiting inductance	1
R_s (Ω)	Series resistance	20
L_s (mH)	Series inductance	8

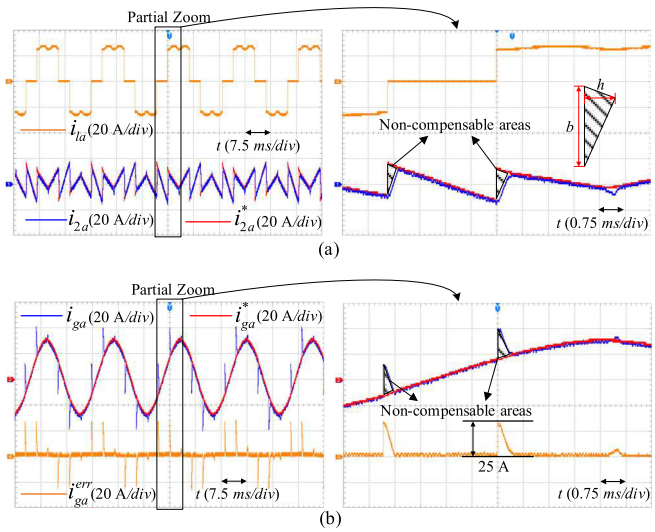

Fig. 15. Steady-state experimental results of nonlinear load without L_{i1}. (a) A-phase load current, SAPF output current, and its reference. (b) A-phase grid current, grid current reference, and their errors.

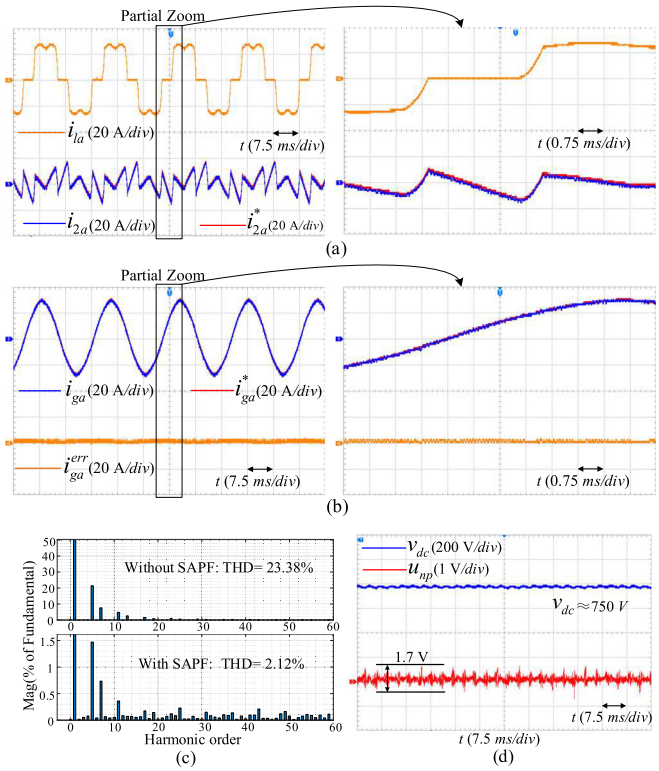

Fig. 16. Steady-state results of the nonlinear load with L_{i1}. (a) Load current, SAPF output current, and its reference. (b) A-phase grid current, grid current reference, and their error. (c) Harmonic distributions of the grid current.(d) DC bus and NP voltages.

topologies lies in the current-limiting inductances L_{i1} that are connected to the uncontrolled rectifier bridge. The load current of the former is periodically changed by the rectifier bridge, as are its harmonic components. In the latter, owing to the nature of the inductance, the current cannot change abruptly. Thus, the lower the inductance, the higher the load/harmonic current change rate.

2) Trouble-Free Operation Without L_{l1}: Fig. 15 shows the steady-state experimental results for the nonlinear load without L_{i1}. As shown in Fig. 15, the abrupt current of the nonlinear load current occurs periodically, similar to its harmonic component. In other words, the SAPF must keep track of an abrupt reference current. The proposed method cannot achieve zero-error tracking of abrupt current changes.

Therefore, noncompensable areas inevitably appear in Fig. 15. The base of the triangular area is determined by the nonlinear load itself, and the height is determined by the dynamic response of the control method. If the nonlinear load remains unchanged, even if the rising time is very small, the grid current compensated by SAPF will retain an upper convex and lower concave, whose heights are equal to the base of each triangular area.

3) Trouble-Free Operation With L_{l1}: Fig. 16 shows the steady-state experimental results for the nonlinear load with L_{i1}. Owing to the current limiting of L_{i1}, the reference current of SAPF did not change rapidly. Therefore, there were no noncompensable areas in the grid current. The grid current not only exhibited a good output but was also guaranteed to be in phase with the grid. Fig. 16(c) shows the harmonic spectrum of the grid current for Phase A. The THD of the grid current without harmonic compensation was 23.38%, and the THD after compensation was only 2.12%, indicating that the proposed strategy had excellent harmonic compensation capabilities in the absence of faults. Fig. 16(d) shows the dc bus voltage (∼750 V) and NP voltage (∼1.7 V). With the adaptive dc bus voltage control, the dc-link voltage could be stabilized automatically without allocating a voltage reference. Meanwhile, the series-connected dc bus capacitors shared the dc bus voltage well. The stability of the dc bus voltage and the balance of the NP voltage ensured a smooth operation.

C. Experiments in Special Cases

To verify the reliability of the proposed control strategy, several special situations for SAPF were also tested; these included unbalanced grid voltages, grid voltages with harmonic components, parameter mismatch, and abrupt load changes. The SAPF is operated under a free fault, and Fig. 14(b) is selected for the nonlinear load.

1) Unbalanced Grid Voltages: Fig. 17 shows the steady-state experimental results under an unbalanced grid voltage, where the voltages of Phases B and C were increased to 110% and decreased to 90% of their nominal values, respectively. Under the influence of an unbalanced grid voltage, the grid currents exhibited a slight imbalance, where the current of Phase B was

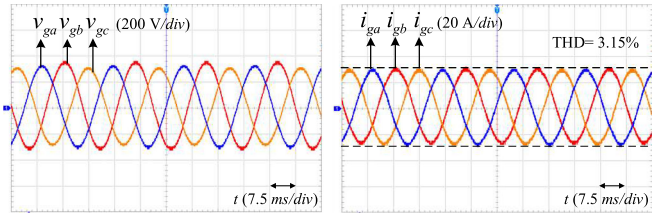

Fig. 17. Steady-state experimental results under unbalanced grid voltages. (a) Three-phase grid voltages. (b) Three-phase grid currents.

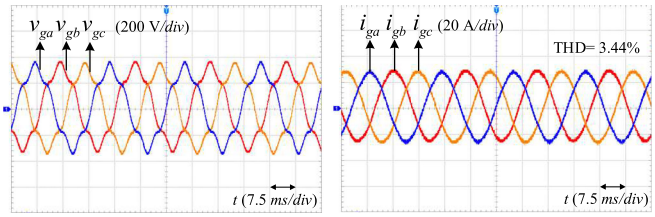

Fig. 18. Steady-state experimental results under unbalanced grid voltages. (a) Three-phase grid voltages. (b) Three-phase grid currents.

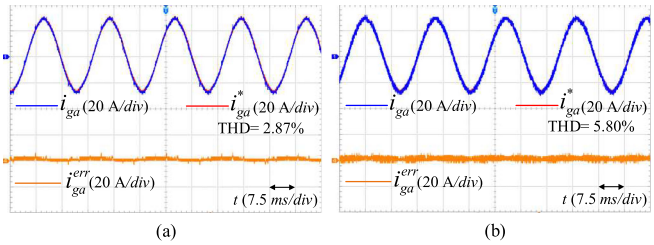

Fig. 19. Steady-state experimental results under filter parameter mismatches. (a) Case I. (b) Case II.

slightly higher than that of Phases A and C. The THD of the grid currents was ∼3.15%.

2) Grid Voltages With Harmonic Components: Fig. 18 shows the steady-state experimental results under a distorted grid voltage, where each phase was injected with 10% fifth harmonics. Despite the distorted grid voltages, the grid currents were still well compensated by a THD of 3.44%.

3) Parameter Mismatch: To verify the robustness of the proposed method, the parameter mismatch of the *LCL* filter in two cases under a healthy state was tested. Case I: The actual *LCL* parameters were 150% of their nominal values, namely, $L_1 = 9$ mH, $L_2 = 15$ μH, and $C_f = 15$ μF. Case II: The actual *LCL* parameters were 50% of their nominal values, namely, $L_1 = 3$ mH, $L_2 = 3$ μH, and $C_f = 3$ μF.

Fig. 19(a) shows the steady-state experimental results for Case I. There are clear high-frequency burrs present in the grid current with a THD equal to 2.87%. Fig. 19(b) shows the results for Case II. The harmonic component of the grid current was relatively high with a THD equal to 5.80%. The FCS-MPC-based method requires the accurate mathematical model; thus, parameter mismatches will lead to changes in the matrices of (6) and alter the control effect. However, the proposed method still shows good robustness under changes in the *LCL* filter parameters.

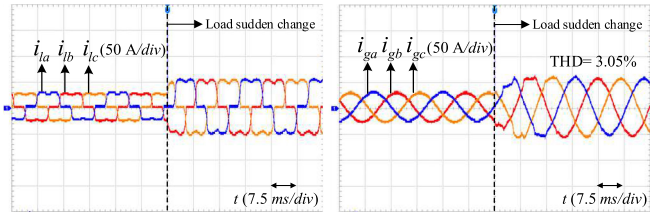

Fig. 20. Experimental results under sudden load change. (a) Three-phase load currents. (b) Three-phase grid currents.

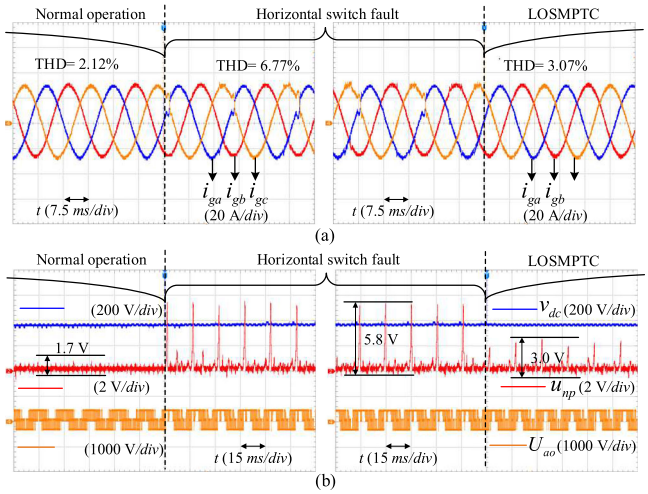

Fig. 21. Experimental results under horizontal switch fault. (a) Three-phase grid currents. (b) DC bus voltage, NP voltage, and A-phase pole voltage.

4) Load Changes: Fig. 20 shows the dynamic response of the load and grid currents under load changes, for the nonlinear load in Fig. 14(b) when L_s and R_s were suddenly reduced to half of its original value. As shown in Fig. 20, after an abrupt increase in load current, the grid currents stabilized with a settling time of ∼1.5 ms, and the THD was 3.05%.

D. Experiments Under Open-Circuit Faults

To demonstrate that the proposed control strategy has a fault-tolerance of horizontal and vertical faults, open-circuit fault experiments of horizontal switch S_{a3} and vertical switch S_{a1} were conducted. The experiments included three scenarios. 1) Normal operation without faults; the SAPF system is in a healthy state. 2) Faults occur but have not been diagnosed; the control system regards the SAPF as being in a healthy state. 3) Faults occur and have been diagnosed; the working state of the system is evaluated in each sampling period, according to the discussion in Section III-B.

1) Horizontal Switch Fault: Fig. 21 shows the experimental results for the horizontal switch fault. When a fault occurred, the three-phase grid currents were distorted to some extent with a THD equal to 6.77% (Phase A, which was the most distorted); however, the distortion was small. The dc bus voltage fluctuated slightly, and the NP voltage had a small fluctuation of 5.8 V. The

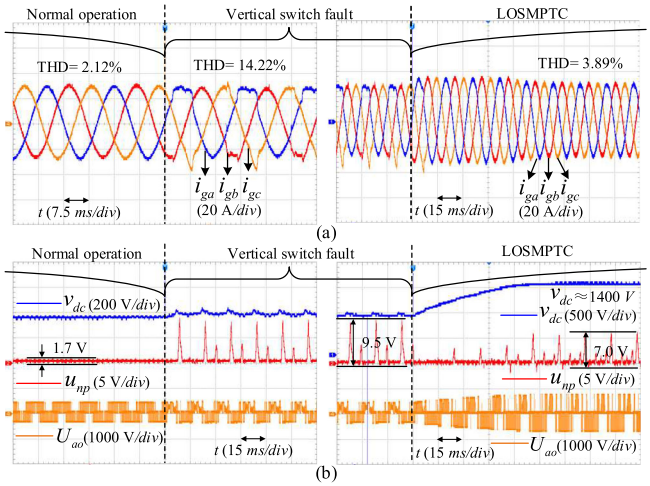

Fig. 22. Experimental results under vertical switch fault. (a) Three-phase grid currents. (b) DC bus voltage, NP voltage, and A-phase pole voltage.

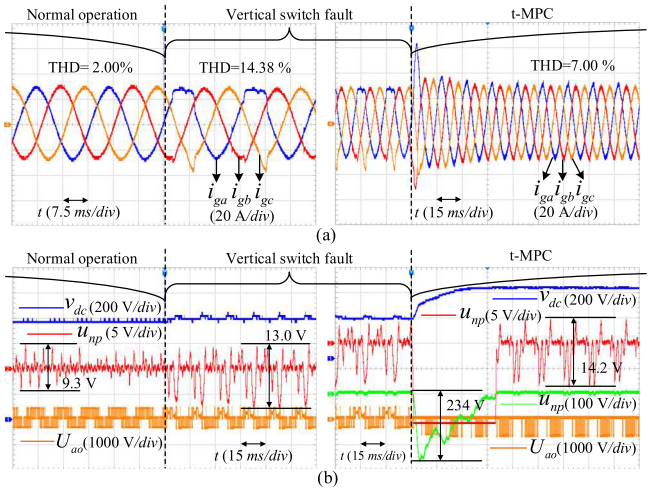

Fig. 23. Experimental results of vertical switch fault using the t-MPC method. (a) Three-phase grid currents. (b) DC bus voltage, NP voltage, and A-phase pole voltage.

pole voltage U_{ao} reflected the switching of the A phase in the three states [P], [O], and [N]. The absence of the [O] states in Fig. 21(b) led to a poor control effect.

After the fault was diagnosed, the LOSMPC could perform fault tolerance control. As shown in Fig. 21, the three-phase grid current quality was better, and the THD was reduced to 3.07%. Second, the fluctuation of the dc bus voltage and NP voltage became smaller (∼3.0 V). Finally, it can be seen from the pole voltage that the fault-tolerant strategy made full use of the [O] state of the healthy state, which improved the power quality of the grid current and NP voltage.

2) Vertical Switch Fault: Fig. 22 shows the experimental results for the vertical switch fault. When a fault occurred, a very large distortion of the three-phase grid currents was observed with a THD equal to 14.12% (Phase A). This was because the modulation range of the vertical switch fault was reduced by half compared to that of the horizontal switch fault. The dc bus voltage fluctuated considerably, and the NP voltage is fluctuated by 8.9 V. The absence of [P] states in the pole voltage U_{ao} in Fig. 21(b) produced a poor control effect.

When a fault is diagnosed, LOSMPC can perform fault tolerance control. To extend the modulation range, the proposed adaptive dc bus voltage control can also improve the voltage reference. In addition, as shown in Fig. 22(b), the dc bus voltage increased from 750 to 1400 V, with a setting time of ∼50 ms. During this period, the current reference for LOSMPC control was incorrect and did not return to normal until the voltage was stabilized. The amplitude of the grid current shown in Fig. 22(a) was initially larger and later returned to normal with a similar setting time of 50 ms.

Despite this, the FTC effect of the system under vertical switch faults remained outstanding. As shown in Fig. 22, the THD of the grid currents was reduced to 3.89%. Second, the fluctuation of the dc bus voltage and NP voltage became smaller (∼7.0 V). Finally, it can be seen from the pole voltage that the fault-tolerant strategy made full use of the [P] state of the healthy state to improve the power quality of the grid current and NP voltage.

To conclude, the proposed LOSMPTC method with adaptive dc bus voltage regulation achieved excellent harmonic compensation and balance of the NP voltage under horizontal or vertical switch faults.

E. Comparison With Existing Methods

1) Experimental Conditions: To verify the superiority of the proposed method in FTC, t-MPC and SMPC experiments under vertical switch faults were compared. For a fair comparison, the experiments (t-MPC and SMPC) were performed under the same conditions as the LOSMPC method.

For t-MPC, we referred to control policies (22) and (23). Before the fault was diagnosed, $\lambda_{\rm np} = 1$, and the set of CVVs contained all 27 CVVs of the healthy state. After the fault was diagnosed, $\lambda_{\rm np} = 10$, and the set of CVVs contained all 18 CVVs of the vertical unhealthy state.

For SMPC, we refer to Algorithm 2; however, n_2 was 5. Before the fault was diagnosed, the SAPF was considered to be in a healthy state. After the fault was diagnosed, the control system judged the working state of each sampling moment according to the principle described in Section III-B.

In addition, no change was observed in the experimental parameters and adaptive dc bus voltage control. As soon as the system at a certain sampling time was identified to be vertically unhealthy, the reference of the dc bus voltage increased to ensure the modulation range. Without special clarification, the THD of the grid currents was the average THD of the three phases.

2) t-MPC Method: Fig. 23 shows the experimental results of the vertical switch fault under the t-MPC control. Before a fault occurred, the THD of the grid currents was only 2.00%, although the NP voltage was relatively large (∼9.3 V). The grid current and NP voltage both deteriorated after the fault with a THD of 14.38% (Phase A) and a fluctuation of 13.0 V. When the fault-tolerance method with t-MPC was applied, the control effects were not satisfactory. Although the setting time of the dc bus voltage was reduced to 30 ms compared with LOSMPC, the

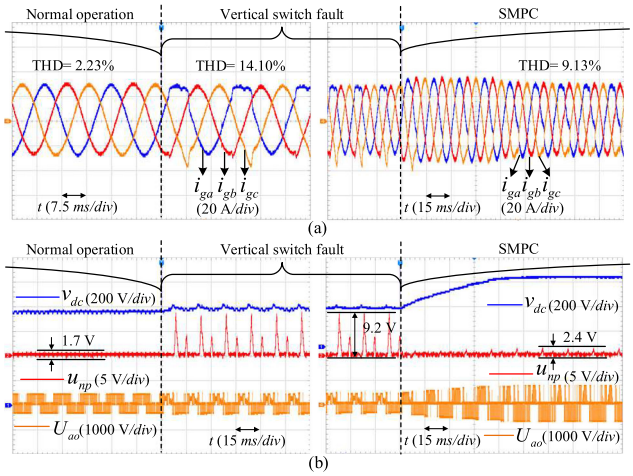

Fig. 24. Experimental results of the vertical switch fault using SMPC method. (a) Three-phase grid currents. (b) DC bus voltage, NP voltage, and A-phase pole voltage.

NP voltage distortion was as high as 234 V during this setting period, and even after the dc bus voltage was stabilized, a 14.2 V fluctuation remained present in the NP voltage. The grid current compensation effect was also limited, and its THD was equal to 7.00% (Phase A, which was the most distorted; the THDs of Phases B and C were ∼5%).

The selection of the weighting factor $\lambda_{\rm np}$ was one reason for the above phenomenon; however, the most important factor is reflected in the pole voltage U_{ao}. The CVVs for t-MPC were always 18 after fault diagnosis, that is, the [P] state of Phase A after fault diagnosis never existed. Therefore, U_{ao} in Fig. 23(b) has only two levels ([O] and [N]) during the FTC period. Proper use of the [P] level is a key factor in ensuring satisfactory fault-tolerant operation of the vertical switch fault.

3) SMPC Method: Fig. 24 shows the experimental results for the vertical switch fault using the SMPC method. Before the fault occurred, the THD of the grid currents was 2.23%, slightly higher than that of the LOSMPC, and the NP voltage was equal to that of LOSMPC (both were 1.7 V). The results indicate that the control effects of the two methods were basically identical when no fault occurred. This can be easily explained as follows. As can be seen in Fig. 11, the mathematical expectation of n_2 for LOSMPC without fault was 4.69, whereas n_2 for SMPC was 5; thus, the control effects were very similar. When a fault occurred, the deterioration degrees of the two methods were also similar. The grid current THD with SMPC was 14.10% (Phase A), and the NP voltage was 9.2 V.

However, after the fault was diagnosed, the fixed weighting number n_2 of the SMPC limited its control effect. Although, like LOSMPC, the [P] states were fully utilized [as seen from the pole voltage in Fig. 24(b)], it did not assign more weight to the grid currents. This resulted in a very small NP voltage of only 2.4 V with a THD of 9.13% of the grid currents (referred to as Phase A, which was seriously distorted. The THD for Phases B and C was ∼6%). In comparison, the noninteger weighting number n_2 in the proposed LOSMPC could handle the fault-tolerance problems of the 3LT^{2}C SAPF more flexibly.

TABLE VI
COMPARISON BETWEEN THE THREE METHODS

	Index	t-MPC	SMPC	LOSMPC
No fault	THD (%)	2.00	2.23	2.12
	u_{np} (V)	9.3	1.7	1.7
Fault occurs	THD (%)	14.38	14.10	14.42
	u_{np} (V)	13.0	9.2	8.9
Fault-tolerance	THD (%)	7.00	9.13	3.89
	u_{np} (V)	14.2	2.4	7.0

4) Summary: Table VI lists the experimental results for the above three methods, namely, no fault, undiagnosed vertical switch fault, and supplementary FTC applied. There was no significant difference between the three methods in terms of trouble-free operation. However, from the perspective of FTC, the proposed LOSMPC was more suitable. First, LOSMPC can make better use of the [P] state to improve the efficiency of the converter when a vertical switch fault occurs. Second, LOSMPC with adaptive dc bus voltage control can achieve a sufficient modulation range. Finally, LOSMPC can choose the weighting number more flexibly; it expressed it as a noninteger at the macroscale, and it could be automatically adjusted.

VII. CONCLUSION

This article proposes a novel nonintegral LO-based SMPTC control strategy to perform FTC of a 3LT^{2}C SAPF under open-circuit faults in both NP switches and half-bridge switches. The strategy was implemented by introducing a cascaded control sequence, that is, the NP voltage was ranked as the highest priority, and the output current of SAPF was ranked as a secondary priority. Thus, compared with t-MPC, SMPTC eliminates the selection of weighting factors. Under fault conditions, the proposed nonintegral SMPTC strategy could realize FTC, achieving excellent harmonic current compensation capability and maintaining the stability of the dc bus voltage and NP voltage. In addition, to simplify the time-consuming dc bus voltage reference specification, an adaptive dc bus voltage regulation method was introduced such that the dc bus voltage could be automatically determined by the nonlinear load. Experimental results further confirm the feasibility and validity of the proposed strategy, which has strong feasibility and can also be applied to other systems (e.g., motor drive systems and multilevel converter systems).

It is needed to note that the proposed scheme is only suitable when only one power transistor faults in 3LT^{2}C APF. If two or more power transistors faults simultaneously, new research work may be investigated. It is suggested that future research can consider the open-circuit FTC control of parallel-connected APF systems.

REFERENCES

[1] M. Aredes, J. Hafner, and K. Heumann, "Three-phase four-wire shunt active filter control strategies," *IEEE Trans. Power Electron.*, vol. 12, no. 2, pp. 311–318, Mar. 1997, doi: 10.1109/63.558748.

[2] Y. Tang, P. C. Loh, P. Wang, F. H. Choo, F. Gao, and F. Blaabjerg, "Generalized design of high performance shunt active power filter with output LCL filter," *IEEE Trans. Ind. Electron.*, vol. 59, no. 3, pp. 1443–1452, Mar. 2012, doi: 10.1109/TIE.2011.2167117.

[3] J. Hurng-Liahng, W. Jinn-Chang, C. Yao-Jen, and F. Ya-Tsung, "A novel active power filter for harmonic suppression," *IEEE Trans. Power Del.*, vol. 20, no. 2, pp. 1507–1513, Apr. 2005, doi: 10.1109/TPWRD.2004.841305.

[4] A. Sheir, M. Z. Youssef, and M. Orabi, "A novel bidirectional T-Type multilevel inverter for electric vehicle applications," *IEEE Trans. Power Electron.*, vol. 34, no. 7, pp. 6648–6658, Jul. 2019, doi: 10.1109/TPEL.2018.2871624.

[5] S. Wang, A. M. Massoud, and B. W. Williams, "A T-Type modular multilevel converter," *IEEE J. Emerg. Sel. Topics Power Electron.*, vol. 9, no. 1, pp. 843–857, Feb. 2021, doi: 10.1109/JESTPE.2019.2953007.

[6] A. Bahrami and M. Narimani, "A sinusoidal pulsewidth modulation (SPWM) technique for capacitor voltage balancing of a nested T-Type four-level inverter," *IEEE Trans. Power Electron.*, vol. 34, no. 2, pp. 1008–1012, Feb. 2019, doi: 10.1109/TPEL.2018.2846618.

[7] K. Komatsu *et al.*, "New IGBT modules for advanced neutral-point-clamped 3-level power converters," in *Proc. Int. Power Electron. Conf. – ECCE Asia*, Sapporo, Japan, 2010, pp. 523–527, doi: 10.1109/IPEC.2010.5543275.

[8] M. Schweizer and J. W. Kolar, "High efficiency drive system with 3-level T-type inverter," in *Proc. 14th Eur. Conf. Power Electron. Appl.*, Birmingham, U.K., 2011, pp. 1–10.

[9] M. Schweizer and J. W. Kolar, "Design and implementation of a highly efficient three-level T-Type converter for low-voltage applications," *IEEE Trans. Power Electron.*, vol. 28, no. 2, pp. 899–907, Feb. 2013, doi: 10.1109/TPEL.2012.2203151.

[10] R. Teichmann and S. Bernet, "A comparison of three-level converters versus two-level converters for low-voltage drives, traction, and utility applications," *IEEE Trans. Ind. Appl.*, vol. 41, no. 3, pp. 855–865, May/Jun. 2005, doi: 10.1109/TIA.2005.847285.

[11] S. Yang, A. Bryant, P. Mawby, D. Xiang, L. Ran, and P. Tavner, "An industry-based survey of reliability in power electronic converters," *IEEE Trans. Ind. Appl.*, vol. 47, no. 3, pp. 1441–1451, May/Jun. 2011, doi: 10.1109/TIA.2011.2124436.

[12] X. Li, S. Dusmez, B. Akin, and K. Rajashekara, "A new SVPWM for the phase current reconstruction of three-phase three-level T-type converters," *IEEE Trans. Power Electron.*, vol. 31, no. 3, pp. 2627–2637, Mar. 2016, doi: 10.1109/TPEL.2015.2440421.

[13] G. H. Li, Y. F. Wang, X. P. Gao, L. Zhang, and L. W. Zhang, "A fault-tolerance method of shunt active power filter based on direct power control," *Meitan Xuebao/J. China Coal Soc.*, vol. 39, no. 12, pp. 2544–2549, 2014.

[14] D. M. Raimondo, G. R. Marseglia, R. D. Braatz, and J. K. Scott, "Fault-tolerant model predictive control with active fault isolation," in *Proc. Control Fault-Tolerant Syst.*, Nice, France, 2013, pp. 444–449.

[15] R. Katebi, J. He, and N. Weise, "Investigation of fault-tolerant capabilities in an advanced three-level active T-type converter," *IEEE J. Emerg. Sel. Topics Power Electron.*, vol. 7, no. 1, pp. 446–457, Mar. 2019, doi: 10.1109/JESTPE.2018.2834367.

[16] Z. J. Ma and S. Thomas, "Reliability and maintainability in photovoltaic inverter design," in *Proc. - Annu. Rel. Maintainability Symp.*, Lake Buena Vista, FL, USA, 2011, pp. 1–5, doi: 10.1109/RAMS.2011.5754523.

[17] U. Choi, J. Lee, F. Blaabjerg, and K. Lee, "Open-circuit fault diagnosis and fault-tolerant control for a grid-connected NPC inverter," *IEEE Trans. Power Electron.*, vol. 31, no. 10, pp. 7234–7247, Oct. 2016, doi: 10.1109/TPEL.2015.2510224.

[18] B. Li, S. Shi, B. Wang, G. Wang, W. Wang, and D. Xu, "Fault diagnosis and tolerant control of single IGBT open-circuit failure in modular multilevel converters," *IEEE Trans. Power Electron.*, vol. 31, no. 4, pp. 3165–3176, Apr. 2016, doi: 10.1109/TPEL.2015.2454534.

[19] B. Wang, Z. Li, Z. Bai, P. T. Krein, and H. Ma, "Real-time diagnosis of multiple transistor open-circuit faults in a T-type inverter based on finite-state machine model," *CPSS Trans. Power Electron. Appl.*, vol. 5, no. 1, pp. 74–85, 2020, doi: 10.24295/CPSSTPEA.2020.00007.

[20] B. Lu and S. K. Sharma, "A literature review of IGBT fault diagnostic and protection methods for power inverters," *IEEE Trans. Ind. Appl.*, vol. 45, no. 5, pp. 1770–1777, Sep./Oct. 2009, doi: 10.1109/TIA.2009.2027535.

[21] Q. Xu, Y. Wang, M. Wang, J. Zhan, and G. Chen, "A novel fault-tolerant control scheme for shunt active power filter with high reliability," in *Proc . IEEE Energy Convers. Congr. Expo.*, Montreal, QC, Canada, 2015, pp. 5531–5537, doi: 10.1109/ECCE.2015.7310438.

[22] D. Zhou and Y. Tang, "A model predictive control-based open-circuit fault diagnosis and tolerant scheme of three-phase AC–DC rectifiers," *IEEE J. Emerg. Sel. Topics Power Electron.*, vol. 7, no. 4, pp. 2158–2169, Dec. 2019, doi: 10.1109/JESTPE.2018.2888879.

[23] X. Qunwei, W. Yue, W. Mian, Z. Jinxiang, S. Zhaohui, and C. Guozhu, "A novel fault-tolerant shunt active power filter and its control strategy," in *Proc. IEEE 24th Int. Symp. Ind. Electron.*, Buzios, Brazil, 2015, pp. 196–201, doi: 10.1109/ISIE.2015.7281468.

[24] U. Choi, F. Blaabjerg, and K. Lee, "Reliability improvement of a T-Type three-level inverter with fault-tolerant control strategy," *IEEE Trans. Power Electron.*, vol. 30, no. 5, pp. 2660–2673, May 2015, doi: 10.1109/TPEL.2014.2325891.

[25] U. Choi, K. Lee, and F. Blaabjerg, "Diagnosis and tolerant strategy of an open-switch fault for T-type three-level inverter systems," *IEEE Trans. Ind. Appl.*, vol. 50, no. 1, pp. 495–508, Jan./Feb. 2014, doi: 10.1109/TIA.2013.2269531.

[26] J. Lee and K. Lee, "Open-circuit fault-tolerant control for outer switches of three-level rectifiers in wind turbine systems," *IEEE Trans. Power Electron.*, vol. 31, no. 5, pp. 3806–3815, May 2016, doi: 10.1109/TPEL.2015.2464803.

[27] J. Chen, C. Zhang, A. Chen, and X. Xing, "Fault-tolerant control strategies for T-type three-level inverters considering neutral-point voltage oscillations," *IEEE Trans. Ind. Electron.*, vol. 66, no. 4, pp. 2837–2846, Apr. 2019, doi: 10.1109/TIE.2018.2842731.

[28] M. Narimani, W. Bin, V. Yaramasu, C. Zhongyuan, and N. R. Zargari, "Finite control-set model predictive control (FCS-MPC) of nested neutral point-clamped (NNPC) converter," *IEEE Trans. Power Electron.*, vol. 30, no. 12, pp. 7262–7269, Dec. 2015, doi: 10.1109/TPEL.2015.2396033.

[29] S. Vazquez, J. Rodriguez, M. Rivera, L. G. Franquelo, and M. Norambuena, "Model predictive control for power converters and drives: Advances and trends," *IEEE Trans. Ind. Electron.*, vol. 64, no. 2, pp. 935–947, Feb. 2017, doi: 10.1109/TIE.2016.2625238.

[30] C. Bordons and C. Montero, "Basic principles of MPC for power converters: Bridging the gap between theory and practice," *IEEE Ind. Electron. Mag.*, vol. 9, no. 3, pp. 31–43, Sep. 2015, doi: 10.1109/MIE.2014.2356600.

[31] M. Norambuena, J. Rodriguez, Z. Zhang, F. Wang, C. Garcia, and R. Kennel, "A very simple strategy for high-quality performance of AC machines using model predictive control," *IEEE Trans. Power Electron.*, vol. 34, no. 1, pp. 794–800, Jan. 2019, doi: 10.1109/TPEL.2018.2812833.

[32] K. Zhang *et al.*, "Tolerant sequential model predictive direct torque control of permanent magnet synchronous machine drives," *IEEE Trans. Transp. Electrific.*, vol. 6, no. 3, pp. 1167–1176, Sep. 2020, doi: 10.1109/TTE.2020.3008828.

[33] J. He, Y. W. Li, F. Blaabjerg, and X. Wang, "Active harmonic filtering using current-controlled, grid-connected DG units with closed-loop power control," *IEEE Trans. Power Electron.*, vol. 29, no. 2, pp. 642–653, Feb. 2014, doi: 10.1109/TPEL.2013.2255895.

[34] F. Ornelas-Tellez, J. J. Rico-Melgoza, R. Morfin-Magaña, and S. Ramos-Paz, "Optimal dynamic harmonic extraction and suppression in power conditioning applications," *IEEE Trans. Ind. Electron.*, vol. 67, no. 9, pp. 7909–7918, Sep. 2020, doi: 10.1109/TIE.2019.2944059.

[35] Y. Zhang, K. Dai, X. Chen, Y. Kang, and Z. Dai, "Stability analysis of SAPF by viewing DFT as cluster of BPF for selective harmonic suppression and resonance damping," *IEEE Trans. Ind. Appl.*, vol. 55, no. 2, pp. 1598–1607, Mar./Apr. 2019, doi: 10.1109/TIA.2018.2872649.

[36] J. Scoltock, T. Geyer, and U. K. Madawala, "Model predictive direct power control for grid-connected NPC converters," *IEEE Trans. Ind. Electron.*, vol. 62, no. 9, pp. 5319–5328, Sep. 2015, doi: 10.1109/TIE.2015.2410259.

[37] J. He, Q. Yang, and Z. Wang, "On-line fault diagnosis and fault-tolerant operation of modular multilevel converters—A comprehensive review," *CES Trans. Elect. Mach. Syst.*, vol. 4, no. 4, pp. 360–372, 2020, doi: 10.30941/CESTEMS.2020.00043.

[38] J. Wang, W. Zhang, W. Jiang, M. Ma, Q. Zhang, and X. Huang, "Application ranges of fault-tolerant control for T-type three-level inverter under single/multi-phase open-circuit faults of inner switches," *IEEE Access*, vol. 8, pp. 207599–207609, 2020, doi: 10.1109/ACCESS.2020.3034919.

[39] Z. Li, B. Wang, Y. Ren, J. Wang, Z. Bai, and H. Ma, "L and LCL-filtered grid-tied single-phase inverter transistor open-circuit fault diagnosis based on post-fault reconfiguration algorithms," *IEEE Trans. Power Electron.*, vol. 34, no. 10, pp. 10180–10192, Oct. 2019, doi: 10.1109/TPEL.2019.2891249.

[40] Y. Zhang, B. Zhang, H. Yang, M. Norambuena, and J. Rodriguez, "Generalized sequential model predictive control of IM drives with field-weakening ability," *IEEE Trans. Power Electron.*, vol. 34, no. 9, pp. 8944–8955, Sep. 2019, doi: 10.1109/TPEL.2018.2886206.

Bo Long (Senior Member, IEEE) received the B.S. degree from Xi'an Petroleum University, Xi'an, China, in 2001, and the Ph.D. degree from Xi'an Jiaotong University, Xi'an, China, in 2008, both in electrical engineering.

In 2008, he joined the Department of Power Electronics, School of Mechatronics Engineering, University of Electronic Science and Technology of China (UESTC), Chengdu, China, and promoted to an Associate Professor in 2014. From 2017 to 2018, he was a Visiting Scholar (Guest Postdoctoral Researcher) in the area of renewable energy and microgrids with the Department of Electrical Engineering, Tsinghua University, Beijing, China. He is currently the Supervisor for 11 master students, two of which have been nominated as provincial outstanding graduate students of UESTC. He has authored more than 20 SCIE-indexed journal papers and one book chapter in the area of power electronics, motor control, battery management system, and smart grid, and he has seven issued and ten pending patents. His research interests include ac/dc microgrids, grid-connected converters for renewable energy systems and DGs, model predictive control, power quality, multilevel converters, ac motor control, and resonance suppression technique for smart grid applications.

Dr. Long is currently an active Reviewer for the IEEE TRANSACTIONS ON POWER ELECTRONICS, *ISA Transactions*, *Applied Energy, Energy*, IEEE TRANSACTIONS ON SMART GRID, IEEE TRANSACTIONS ON INDUSTRIAL ELECTRONICS, IEEE TRANSACTIONS ON SUSTAINABLE ENERGY, and IEEE TRANSACTIONS ON ENERGY CONVERSION.

TianXu Cao (Student Member, IEEE) received the B.S. degree in electrical engineering in 2020 from the University of Electronic Science and Technology of China, Chengdu, China, where he is currently working toward the M.S. degree in mechanical engineering.

His current research interests include the optimization of direct microgrids, involving virtual inertia control, fault-tolerant control of power converters, model predictive control, fractional-order systems, and reliability of power electronic system.

XinYue Qi was born in Harbin, China, in 1997. She received the B.S. degree in electrical engineering from Northeast Petroleum University, Daqing, China, in 2020. She is currently working toward the M.S. degree in flight vehicle design with Tenth Academy, China Aerospace Science and Industry Corporation, Beijing, China.

Her research interests include power electronics and electrical drives, active power filter, predictive control, and sustainable energy systems.

Dawei Sheng received the B.S. degree in smart grid information engineering from the Nanjing University of Posts and Telecommunications, Nanjing, China, in 2019. He is currently working toward the M.S. degree in mechanical engineering with the University of Electronic Science and Technology of China, Chengdu, China.

His current research interests include model predictive control of power converters, passive-based control, power loss minimization of power converters, and microgrids system.

Josep M. Guerrero (Fellow, IEEE) received the B.S. degree in telecommunications engineering, the M.S. degree in electronics engineering, and the Ph.D. degree in power electronics from the Technical University of Catalonia, Barcelona, Spain, in 1997, 2000, and 2003, respectively.

Since 2011, he has been a Full Professor with the Department of Energy Technology, Aalborg University, Aalborg, Denmark, where he is responsible for the Microgrid Research Program. Since 2014, he has been a Chair Professor with Shandong University, Jinan, China. Since 2015, he has been a Distinguished Guest Professor with Hunan University, Changsha, China. Since 2016, he has been a Visiting Professor Fellow with Aston University, Birmingham, U.K., and a Guest Professor with the Nanjing University of Posts and Telecommunications, Nanjing, China. In 2019, he became a Villum Investigator by The Villum Fonden, which supports the Center for Research on Microgrids, Aalborg University, being the Founder and Director of the same center (www.crom.et.aau.dk). He has authored or coauthored more than 600 journal papers in the fields of microgrids and renewable energy systems, which are cited more than 50 000 times. His research interests include different microgrid aspects, including power electronics, distributed energy-storage systems, hierarchical and cooperative control, energy management systems, smart metering, and the Internet of Things for ac/dc microgrid clusters and islanded microgrids, especially focused on microgrid technologies applied to offshore wind, maritime microgrids for electrical ships, vessels, ferries, and seaports, and space microgrids applied to nanosatellites and spacecrafts.

Prof. Guerrero is an Associate Editor for a number of IEEE Transactions. He was the recipient of the Best Paper Award of the IEEE TRANSACTIONS ON ENERGY CONVERSION in 2014–2015, the Best Paper Prize of IEEE Power and Energy Society in 2015, and the Best Paper Award of the *Journal of Power Electronics* in 2016. During six consecutive years, from 2014 to 2019, he was awarded by Clarivate Analytics (former Thomson Reuters) as Highly Cited Researcher with 50 highly cited papers. In 2015, he was elevated as IEEE Fellow for his contributions on "distributed power systems and microgrids."

José Rodríguez (Life Fellow, IEEE) received the Engineering degree from the Universidad Tecnica Federico Santa Maria, Valparaiso, Chile, in 1977, and the Dr.Ing. degree from the University of Erlangen, Erlangen, Germany, in 1985, both in electrical engineering.

Since 1977, he had been with the Department of Electronics Engineering, Universidad Tecnica Federico Santa Maria, where he was a Full Professor and President. From 2015 to 2019, he was the President and a Full Professor with Universidad Andres Bello in Santiago, Santiago, Chile. He has coauthored two books, several book chapters, and more than 400 journal and conference papers. His research interests mainly include multilevel inverters, new converter topologies, control of power converters, and adjustable-speed drives.

Dr. Rodríguez was the recipient of the number of best paper awards from journals of the IEEE. He is a Member of the Chilean Academy of Engineering. He was the recipient of the National Award of Applied Sciences and Technology from the Government of Chile in 2014 and the Eugene Mittelmann Award from the Industrial Electronics Society of the IEEE in 2015. From 2014 to 2020, he has been included in the list of Highly Cited Researchers published by the Web of Science.

Kil To Chong (Member, IEEE) received the Ph.D. degree in mechanical engineering from Texas A&M University, College Station, TX, USA, in 1995.

He is currently a Professor and the Department Head of the School of Electronics and Information Engineering and a member and the Head of the Advanced Electronics and Information Research Center, Chonbuk National University, Jeonju, South Korea. His research interests include motor fault detection and control, network system control, sensor network systems, time-delay systems, and neural networks.